J. Fluid Mech. (1995), *vol.* 303, *pp.* 23–53

Experimental study of interfacial long waves in a two-layer shear flow

By PIERRE BARTHELET, FRANÇOIS CHARRU AND JEAN FABRE

Institut de Mécanique des Fluides, 2, allée du Professeur C. Soula, 31400 Toulouse, France

(Received 28 January 1995 and in revised form 24 June 1995)

Interfacial stability of two-layer Couette flow was investigated experimentally in a channel bent into an annular ring. This paper is focused on the supercritical long-wave instability which arises for a broad range of flow parameters. Above the critical upper plate velocity, a slowly growing long wave appears with wavelength equal to the perimeter of the channel. Transients of this wave were studied within the theoretical frame of amplitude equations obtained from the long-wave interface equation. Near the onset of instability, the unstable fundamental harmonic is described by the Landau–Stuart equation, and the nonlinear dynamics of the harmonics closely follows the central and slaved modes analysis. For the higher upper plate velocity, harmonics gain some autonomy but they eventually are enslaved by the fundamental, through remarkable collapses of amplitudes and phase jumps leading to wave velocity and frequency locking. Dispersive effects play a crucial role in the nonlinear dynamics. Far from the threshold, the second harmonic becomes unstable and bistability appears: the saturated wave is dominated either by the fundamental harmonic, or by the even harmonics, after periodic energy exchange.

1. Introduction

This paper describes a study of the stability of the interface between two superposed viscous layers in plane Couette or Poiseuille flow (figure 1). This problem primarily concerns low Reynolds number flows, but it also provides some essential ideas about the instability mechanisms involved in sheared interfaces. This problem has been investigated in numerous theoretical studies since Yih's (1967) work; in contrast, very few experimental results are available. To our knowledge, only two papers have been published, and both concern Poiseuille flows of oil and water in horizontal channels of rectangular cross-section.

Charles & Lilleleht (1965) showed that the presence of the second fluid affects the transition to turbulence of the first fluid. More precisely, a small flow rate of oil delays the transition to turbulence in the water, while an already turbulent water flow lowers the critical Reynolds number for the oil flow. The transition to turbulence is associated with short interfacial waves, travelling at the same velocity as the patches of turbulence in the water. Increasing the Reynolds number leads to large two-dimensional waves and to roll waves, which propagate much slower than the water.

Kao & Park (1972) studied spatial growth rates of artificially as well as naturally excited shear waves, together with vertical distributions of the amplitude and phase of these disturbances. They were able to plot the neutral stability curve in (Re, k)-plane, where Re is the Reynolds number of the water and k is the wavenumber of the

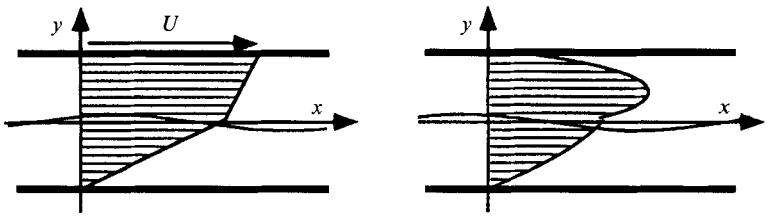

FIGURE 1. Plane two-layer Couette flow (left) and Poiseuille flow (right).

disturbance. The critical Reynolds number agrees with that of Charles & Lilleleht. When a vibrating ribbon was placed close to the interface, true interfacial modes were excited, but they were always found to be damped under the flow conditions explored. The characteristic of these interfacial modes was the strong decay of their amplitude away from the interface, while shear modes were symmetric with respect to the mid-depth of the water.

It should be noted that in these two experimental studies of Poiseuille flow, the interfacial perturbations were induced by the turbulence in one fluid layer. In contrast, for two-layer Couette flow no experimental results are available.

Despite a lack of experimental data, numerous theoretical studies have been carried out. For Poiseuille flow, the linear stability problem was first solved by Yih (1967) for long waves, and then numerically by Yiantsios & Higgins (1988), for arbitrary wavenumber. These latter authors identified the critical Reynolds number for the interfacial mode as being well above the range of Reynolds numbers explored by Kao & Park. This could explain why Kao & Park did not observe any interfacial instability. Nevertheless, the predicted critical Reynolds number for the transition to turbulence was found to be even greater: more than seven times the experimental one! Yiantsios & Higgins suggests that such a dramatic discrepancy could be explained either by the sidewall effects in the experiments (although the aspect ratio of Kao & Park was 1:8), or by nonlinear subcritical instability.

For plane Couette flow, Yih showed that the basic flow may be unstable to long-wavelength disturbances for arbitrarily small Reynolds numbers, owing to viscous stratification, when gravity is not sufficiently stabilizing. Stability to disturbances with wavenumber $kh_1 = O(1)$ (where h_1 is the thickness of the lower layer) was investigated numerically by Renardy (1985, 1987). She showed the existence of a low critical Reynolds number for these $kh_1 = O(1)$ disturbances, for parameter values corresponding to long-wave stability. Hooper & Boyd (1983) showed the existence of a short-wave instability but, as pointed out by Hinch (1984), this instability is always overcome by the stabilizing effect of surface tension. Finally, Hooper & Boyd (1987) showed that the flow can be unstable to 'Tollmien–Schlichting type' waves when one viscous lengthscale is short compared with both the wavelength and the thickness of the lower layer.

A physical mechanism for the short-wave instability has been proposed by Hinch (1984). This mechanism is based on diffusion and convection of the vorticity generated at the sheared interface by velocity disturbances. However, the physical mechanism for the long wave and the $kh_1 = O(1)$ instabilities remains unclear. The long-wave mechanism proposed by Smith (1990) for free falling films is appealing, but it accounts for neither the crucial role played by the viscosity ratio, nor the stabilizing or destabilizing influence of the walls. An analysis involving the energy equation, such as that made by Kelly *et al.* (1989) for free falling films, would shed some light on these questions.

The nonlinear behaviour of long waves has been examined using perturbation methods and bifurcation theory. The leading equation for interfacial long waves with high surface tension is the Kuramoto–Sivashinsky (KS) equation (Hooper & Grimshaw 1985; Shlang *et al.* 1985). Hooper & Grimshaw showed by numerical integration of the KS equation that periodic waves can be sustained when the fundamental harmonic, or the first two harmonics, are the only unstable modes, the other harmonics being stabilized by surface tension. Inspired by the theoretical work of Cohen *et al.* (1976), they interpreted these nonlinear waves as a 'two modes equilibrium' or as a 'bouncy state'. The two modes equilibrium corresponds to an unstable harmonic stabilized by the energy that it supplies to a stable higher harmonic. The bouncy state has been shown to correspond to an intermittent solution where a two-mode equilibrium periodically vanishes and rises again, with its phase shifted by $\pi/2$ (Kevrekidis, Nicolaenko & Scovel 1990; Demekhin, Tokarev & Shkadov 1991).

However, the usefulness of the KS equation for describing long interfacial waves is questionable for two reasons. The first is that this equation involves small Weber number, namely $We = O((kh_1)^2)$, which is only valid for very thin films. The second reason is that the KS equation does not involve any dispersive term, but Chang, Demekhin & Kopelevich (1993) have shown that linear dispersion tends to arrest irregular behaviour and promotes stationary spatially periodic waves, in agreement with experiments on falling films (Liu, Paul & Gollub 1993). These two deficiencies of the KS equation for describing long interfacial waves have been overcome by Charru & Fabre (1994): they included the next order in the long-wave parameter, by which linear dispersion is taken into account, with a less restrictive condition on the Weber number, i.e. $We = O(kh_1)$.

Apart from the above studies, Renardy (1989) derived the Landau–Stuart equation for the amplitude of the marginally stable interfacial mode, using bifurcation theory. She showed that linearly unstable waves with wavenumber $kh_1 = O(1)$ may saturate, corresponding to supercritical bifurcation.

Experimental work for two-layer Couette flow is therefore needed, to confirm the existence of these predicted interfacial instabilities, and to test the value of existing nonlinear studies; these are the objectives of this paper. An experimental device has been designed which overcomes the difficulty of constructing a suitable straight channel, and yet is appropriate for nonlinear wave studies. This device and the basic flow are described in §2. The experimental evidence for long-wave and $kh_1 = O(1)$ instabilities is reported in §3, along with the corresponding marginal stability results. Saturated waves are described in §4. The rest of the paper is devoted to the long wave; short-wave dynamics are left for a later paper. In §5, within the theoretical frame of amplitude equations for spatially confined systems, the transients of the supercritical long wave are studied. The results are finally summarized and discussed in §6.

2. Experimental set-up and basic flow

2.1. *Experimental device and instrumentation*

The difficulty of achieving Couette flow in a straight channel comes from the realization of the upper wall motion, and from the set-up length of the basic flow. These difficulties have been overcome by bending a channel of rectangular cross-section into a ring, so that its ends meet (figure 2). The rotation of the rigid upper plate around the axis of the ring drags the fluids. However, owing to the radial velocity gradient and centrifugal inertia forces, the velocity field may be distorted and further instability generated. The dimensions of the channel were set to minimize these

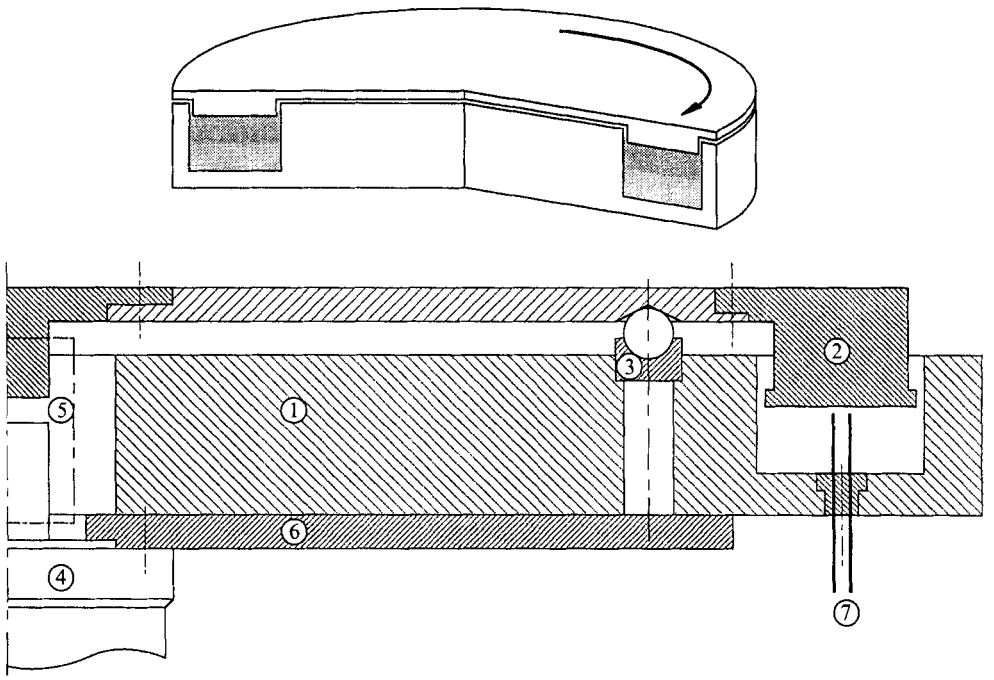

FIGURE 2. Sketch of the experimental device. See text for description.

drawbacks. This arrangement has the following advantages: shearing is achieved by a rigid plate without any vibrations, flows are fully developed without any entry or discharge sections, and wave evolution can be observed over long periods of time. Moreover, the maximum allowed wavelength is equal to the perimeter of the channel, and all waves are expected to be spatially periodic.

The channel is grooved in a Plexiglas plate 1 (figure 2) lying on the support 6. Its mean diameter is $D = 400$ mm so that the radial acceleration is less than 1% (resp. 10%) of gravity for upper plate velocities less than 0.14 m s^{-1} (resp. 0.44 m s^{-1}). The width W of the channel is 40 mm, and its depth H is 20 mm. The rotating plate 2 consists of a Plexiglas crown screwed on an aluminium disk. It is guided by three balls 3 distributed at 120° of each other on the plate 1. The upper plate is driven by a vertical DC servomotor 4 through a flexible coupling 5. Air bubbles created during the filling of the channel can be removed by suction with a syringe through two small holes bored in the upper plate.

The interface position is measured with two conductance probes 7, located at the mid-cross-section, taking advantage of the contrast in conductivities of the two fluids. Each probe is made of two stainless steel wires, separated by $\delta = 3$ mm. The diameter and the length of these electrodes are 0.3 and 18 mm respectively. The wake of the probes is less than 5 cm long, and induces negligible disturbances under the explored flow conditions. The distance between the probes is 307 mm, so that there is no electrical coupling. These local probes respond linearly to interface deflections, and do not generate harmonics. They integrate the interface height over space, and thus behave as a low-pass filter with a gain of $\exp(k\delta/2)$. The resulting attenuation is negligible for the observed waves.

The exploration of the dependence of wave evolution on upper plate velocity is monitored and controlled by a computer. A given velocity level is reached from rest

Fluid	Label	μ (Pa s)	ρ (kg m^{-3})	γ (Pa m)	$m = \mu_2/\mu_1$	$r = \rho_2/\rho_1$
Bayole 82 (mineral oil)	2	0.0297	846	—	—	—
Water–Glycerine (15–85 %)	1a	0.111	1214	0.030	0.268	0.697
Water–Glycerine (32–68 %)	1b	0.0191	1169	0.030	1.55	0.724
Water–Glycerine (37–63 %)	1c	0.0121	1155	0.030	2.45	0.732
Water–Glycerine (42–58 %)	1d	0.0108	1142	0.030	2.76	0.741

TABLE 1. Physical fluid properties at $T = 20$ °C

with an acceleration of about 1 mm s^{-2}. The interface position recording starts when the basic flow is established a few seconds later, and may last for one hour. A typical measurement cycle comprises a succession of increasing and decreasing velocity ramps and levels. Temperature is measured with a thermocouple fixed at the bottom of the channel, and does not vary during a run. More details on the experimental device can be found in Charru (1991).

However small the upper plate velocity, time records show a small-amplitude wave, barely visible to the naked eye, with a frequency equal to the rotation frequency $f \equiv U/\pi D$ of the upper plate. This wave corresponds to the forcing of the interface by the geometrical imperfections of the channel and is not caused by an instability. This parasitic wave does not alter interfacial instabilities and has been systematically eliminated by stop-band filtering. Indeed, any nonlinear interaction would appear on spectra as peaks with frequencies equal to linear combinations of the forcing frequency and free-wave frequencies: such peaks cannot be detected on spectra.

2.2. *Working fluids*

Several combinations of fluids have been tested in order to vary the viscosity ratio. The upper fluid is a mineral oil (Bayole 82, Esso). The lower fluid is a mixture of distilled water and glycerine, whose viscosity (and density to a lesser degree) depends on their proportions. Appropriate conductivity for the water–glycerine mixture was obtained by adding potassium chloride. The physical properties of these fluids are indicated in table 1. The variation of the viscosities with temperature was determined with a Carrimed rheometer in the range 16–24 °C. Although viscosities decrease by about 50 % in this range, their ratio remains approximately constant. Finally, the surface tension γ was measured with a TD1 Lauda device: it appears to be independent of the composition of the water–glycerine mixture.

2.3. *Dimensionless parameters*

The plane Couette flow of two superposed layers involves six independent dimensionless parameters. They are the layer thickness ratio d, the viscosity ratio m and the density ratio r, together with one Reynolds number, one Froude number and one Weber number, defined as follows:

$$d = \frac{h_2}{h_1}; \quad m = \frac{\mu_2}{\mu_1}; \quad r = \frac{\rho_2}{\rho_1}; \quad Re_1 = \frac{h_1 U_I}{\nu_1}; \quad Fr = \frac{U_I^2}{(1-r) g h_1}; \quad We = \frac{\rho_1 h_1 U_I^2}{\gamma}, \tag{1}$$

where subscripts 1 and 2 refer to the lower and upper fluids respectively, and where U_I is the interface velocity linked to the upper plate velocity U through:

$$U_I = \frac{mU}{m+d}. \tag{2}$$

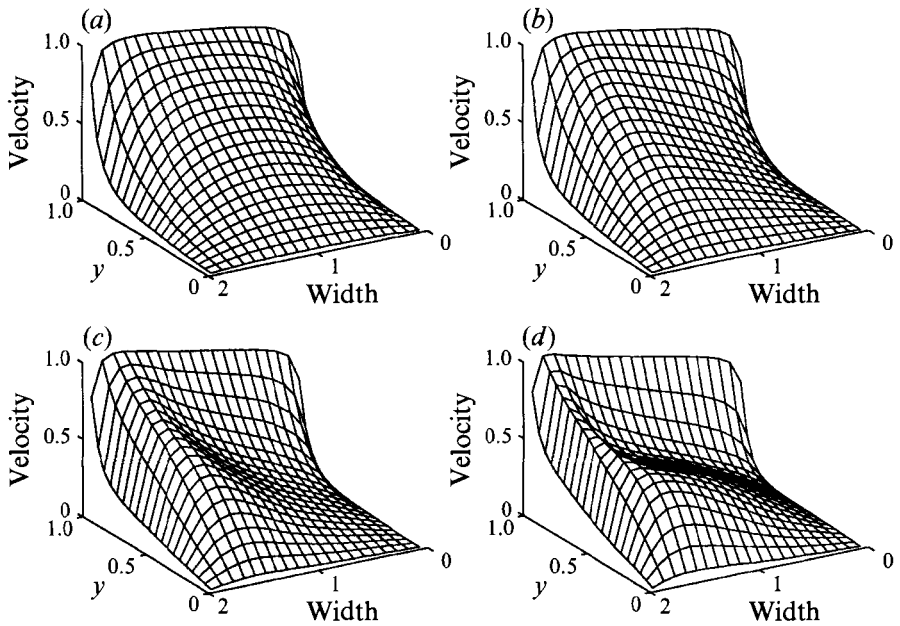

FIGURE 3. Azimuthal velocity field in the cross-section of the channel, for aspect ratio $W/H = 2$, and for $Re = 25$, 100, 200, 500 (*a–d*).

The values of m and r for the working fluids are given in table 1. The Reynolds number Re_2 for the upper fluid can be expressed with the above parameters, from continuity of the shear stress across the interface:

$$Re_2 = \frac{h_2(U-U_I)}{\nu_2} = \frac{rd^2}{m^2} Re_1. \tag{3}$$

2.4. *Basic flow*

The velocity field of the basic flow in the annular ring has been investigated both numerically and experimentally. The numerical study was carried out for a single-phase flow by numerical simulation of the time-dependent Navier–Stokes equations based on the finite volume method (Magnaudet, Rivero & Fabre 1995). The experimental study was performed by laser-Doppler velocimetry (LDV), for both single-phase and two-phase flows. Only measurements of the azimuthal velocity are reported here. The low concentration of particles due to sedimentation allowed only the sign of the radial and vertical components of the velocity to be measured.

For a single-phase flow, figure 3 shows the azimuthal velocity field in the cross-section of the channel obtained by numerical simulation, for Reynolds numbers $Re = UH/\nu$ ranging from 25 to 500, where U is the upper plate velocity in the middle of the channel. It appears that, for $Re = 25$, the vertical velocity profile is linear in the middle half of the span of the channel. For $Re > 100$, the flow is no longer symmetric, with higher velocities near the outer sidewall, and the vertical velocity profiles exhibit an inflexion point for $Re > 200$. Figure 4 shows isovalues of the azimuthal velocity and the secondary flow in the cross-section of the channel, for $Re = 100$. The maximum velocity of the secondary flow is less than $0.07U$. These calculations are confirmed by measurements of the azimuthal velocity, as shown in figure 5. Thus, for $Re < 25$, the

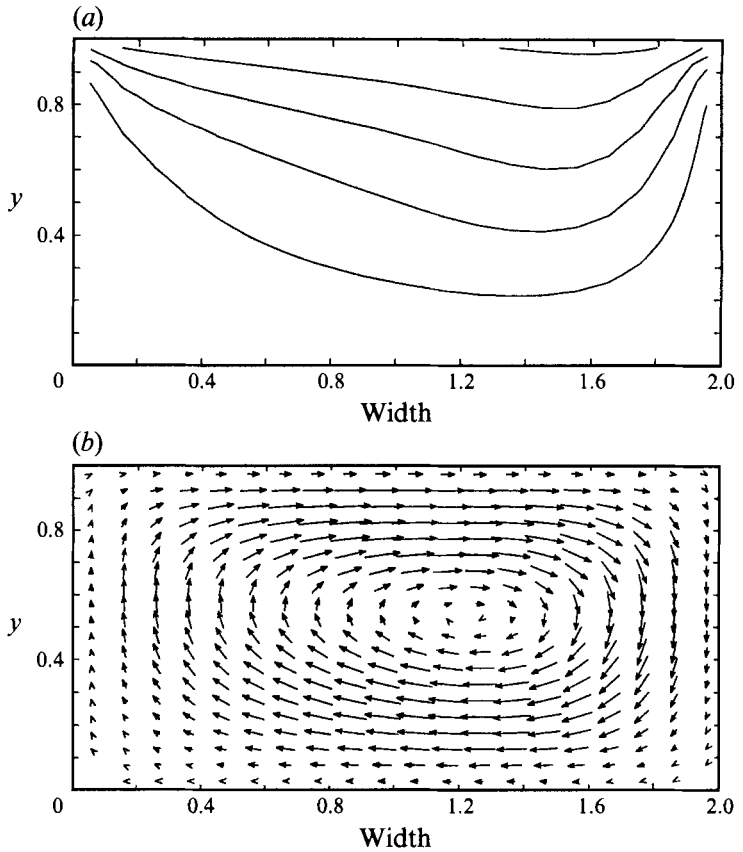

FIGURE 4. Isovalues of the azimuthal velocity (*a*) and secondary flow (*b*) in the cross-section of the channel for $Re = 100$. The isovalues correspond to 0.2, 0.4, 0.6, 0.8 and 1 times the upper plate velocity U in the middle of the channel. The maximum velocity of the secondary flow is less than $0.07U$.

flow is close to plane Couette flow in the middle half of the span of the channel. Finally, as the code allows time-dependent solutions to be captured, it must be pointed out that no instability occurred for $Re < 1000$.

The basic two-phase flow has only been investigated experimentally, owing to the difficulty of numerical simulation of a deformable interface. Figure 6 compares the theoretical plane Couette flow to measurements of the vertical profile of the azimuthal velocity in the middle of the channel, for four values of the Reynolds number. These experimental Reynolds numbers were defined with the estimated interfacial velocity given by (2). No measurement could be performed in the red-coloured upper fluid. Assuming a linear velocity profile in this upper layer, it can be checked that the ratio of the velocity gradients at the interface is equal to the inverse of viscosity ratio, as predicted by continuity of shear stress for plane flow. The higher value of these velocity gradients shows a higher shear stress at the interface and corresponds to enhanced dissipation due to the secondary flow. For $Re_1 = 47$, the experimental and theoretical profiles are close, but for larger Reynolds numbers, the actual velocity is smaller than the theoretical one. (Note that the experimental Reynolds number is defined with the estimated interfacial velocity given by (2).) We have verified that for $Re_1 = 47$, the flow remains close to plane Couette flow in the middle half of the span of the channel.

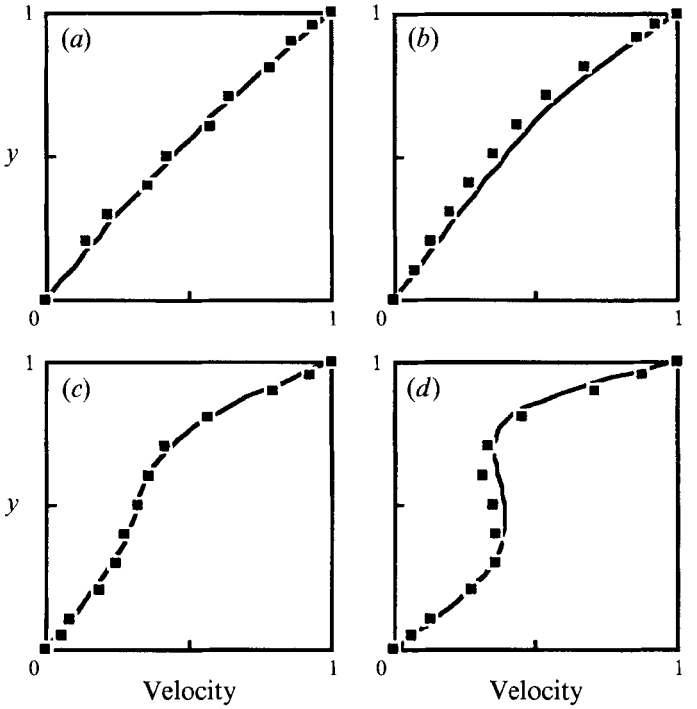

FIGURE 5. Vertical profiles of the azimuthal velocity in the middle of the channel for the single-phase flow: numerical simulation (——) and measurements (■) for $Re = 25$, 100, 200, 500 (*a–d*). Velocity and depth are normalized with the upper plate velocity and total depth.

Finally, experimental investigation of the two-phase flows shows that the basic flow in the middle half of the span of the channel differs by less than 10% from plane Couette flow, for Reynolds number Re_1 smaller than 50.

3. Marginal stability results

3.1. *The two kinds of waves*

At small upper plate velocities, the interface remains flat. When the plate velocity is increased, two kinds of waves with quite different wavelength are observed, depending on the values of the viscosity and thickness ratios m and d.

The first wave is characterized by a wavelength equal to the perimeter of the channel (i.e. $\lambda = \pi D = 1257$ mm), which corresponds to a dimensionless wavenumber $kh_1 = 2\pi h_1/\lambda \approx 0.05$. This wave will be referred to as 'the long wave'. Figure 7(*a*) shows time records of the position of the interface, below and above the critical upper plate velocity U_L (where the subscript L refers to the long wave). The frequency of this wave is rather low, around 0.1–0.3 Hz, and its amplitude is a few tenths of a millimetre. The order of magnitude of the critical velocity is around 0.1–0.6 m s^{-1}, which corresponds to Reynolds numbers of about 100–500 for the less viscous fluid. As will be shown in §4, this bifurcation is generally supercritical. However, for thickness ratios typically close to one, the bifurcation is subcritical, with hysteresis and a finite jump of the amplitude at the threshold.

The wavelength of the second wave is about 40 mm, which is comparable to the depth of the channel, and corresponds to a dimensionless wavenumber

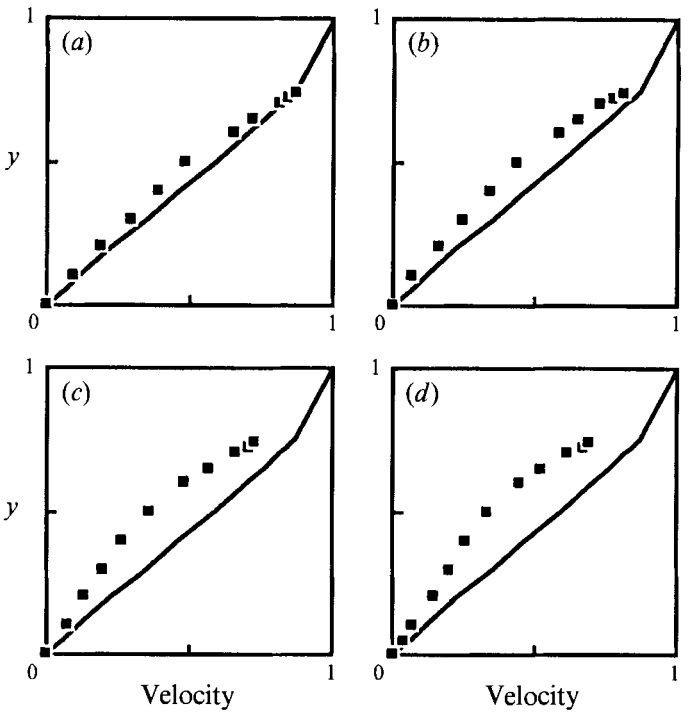

FIGURE 6. Vertical profiles of the azimuthal velocity in the middle of the channel for the two-phase flow: plane Couette flow (——) and measurements (■) for $Re_1 = 47, 97, 190$ and 237 (*a–d*) ($m = 2.2$, $d = 0.33$). Velocity and depth are normalized with the upper plate velocity and the total depth.

$k = 2\pi h_1/\lambda = O(1)$. Figure 7(*b*) displays time records of this wave, which will be referred to as 'the short wave' for simplicity, although it is not strictly a short wave. The frequency of this wave is about 7 Hz. The critical upper plate velocity U_S (where the subscript S refers to the short wave) and the corresponding Reynolds numbers are slightly higher than for the long wave. Within the explored flow conditions, this bifurcation was always supercritical.

The short wave can appear when the long wave is already present, leading to the superposition of the two waves, as shown in figure 7(*c*). The short wave first grows on the crest of the long wave, then spreads all over the interface, and finally 'kills' the long wave.

3.2. *Marginal stability curves*

Figure 8 shows the critical upper plate velocities versus the thickness ratio d, for three different viscosity ratios $m > 1$, corresponding to the upper fluid being more viscous than the lower. Qualitative features of the marginal stability curves are the same for the three viscosity ratios.

For small d (small upper layer thickness), the long wave appears first. As the upper plate velocity is increased further, the short wave appears on the crest of the long wave as shown in figure 7(*c*). For greater thickness ratios, the two critical velocities U_L and U_S are larger, but their difference is smaller, such that the two marginal curves intersect for some $d < 1$. This explains why the short wave first appears on the crest of the long wave: indeed, on the long-wave crest, the local thickness ratio is smaller, and thereby the critical velocity U_S is smaller too.

Above the intersection point, the short wave appears first. Once this short wave is

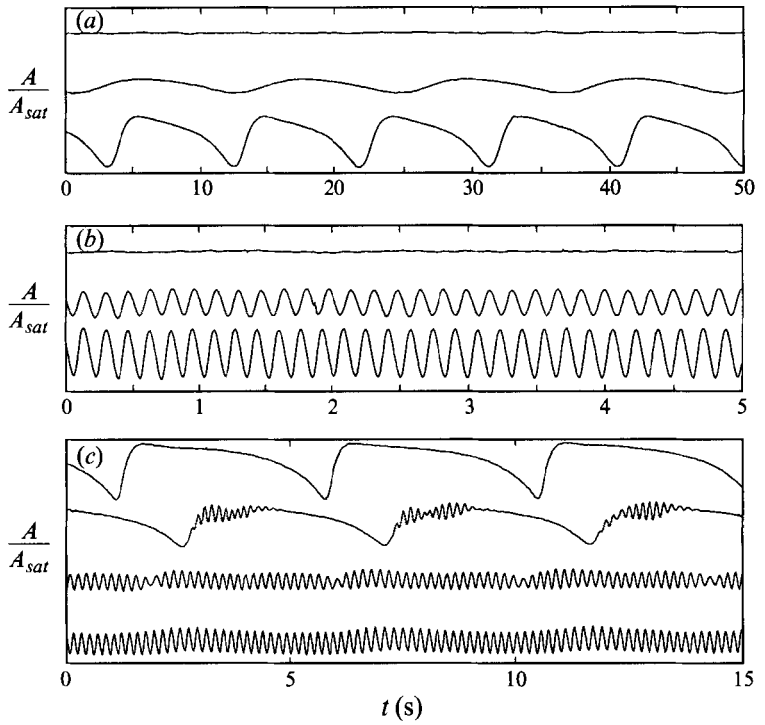

FIGURE 7. Time evolution of the interface position. (*a*) Long wave for $U/U_L = 0.97$, 1.06, 1.33, $U_L = 0.138$ m s^{-1}, fluids (1d–2), $d = 0.25$. (*b*) Short wave for $U/U_S = 0.995$, 1.01, 1.07, $U_S = 0.575$ m s^{-1}, fluids (1b–2), $d = 0.42$. (*c*) Short wave arising on the long wave and then killing it. $U/U_L = 2.63$, 2.71, 2.76, 2.80, $U_S/U_L = 2.65$, $U_L = 0.185$ m s^{-1}, fluids (1b–2), $d = 0.25$.

established, no long wave has been observed. This could mean either that the short wave prevented the growth of the long wave, or that the critical velocity for the long wave had not been reached.

The variation of the long-wave velocity with the thickness ratio and the viscosity ratio are presented in figure 9. The dimensionless wave velocity c/U_L decreases for increasing d and decreasing m. The actual interface velocity U_I can be estimated from LDV measurement for one case only (figure 6); for this case, the wave velocity is close to $c \approx 0.93U_I$.

3.3. *Comparison with linear stability theory*

The above results can be compared with the solution of the linear stability problem for the plane Couette flow (Orr–Sommerfeld equations). This problem was first solved for long waves by Yih (1967), then for short waves by Hooper & Boyd (1983, 1987), and by a numerical method by Renardy (1985).

Taking the lower layer thickness h_1 and the interface velocity U_I as characteristic scales, the dimensionless angular frequency ω and growth rate σ for long waves are

$$\omega = kc_0 - k^3 M, \quad \text{with} \quad c_0 = 1 + L(m,d), \quad M = M(m,d), \tag{4a}$$

$$\sigma = Re_1 k^2 \left\{ R - \frac{k^2 S}{We} \right\}, \quad \text{with} \quad R = R_0(m,d,r) - \frac{S}{Fr}, \quad S = S(m,d), \tag{4b}$$

where c_0 is the wave velocity for $k = 0$. The dispersive term $M(m,d)$ has been calculated by Charru & Fabre (1994). The coefficient $S(m,d)$ is positive for any value of m and d. For flow conditions such that $R_0(m,d,r) < 0$, the flat interface is stable for any

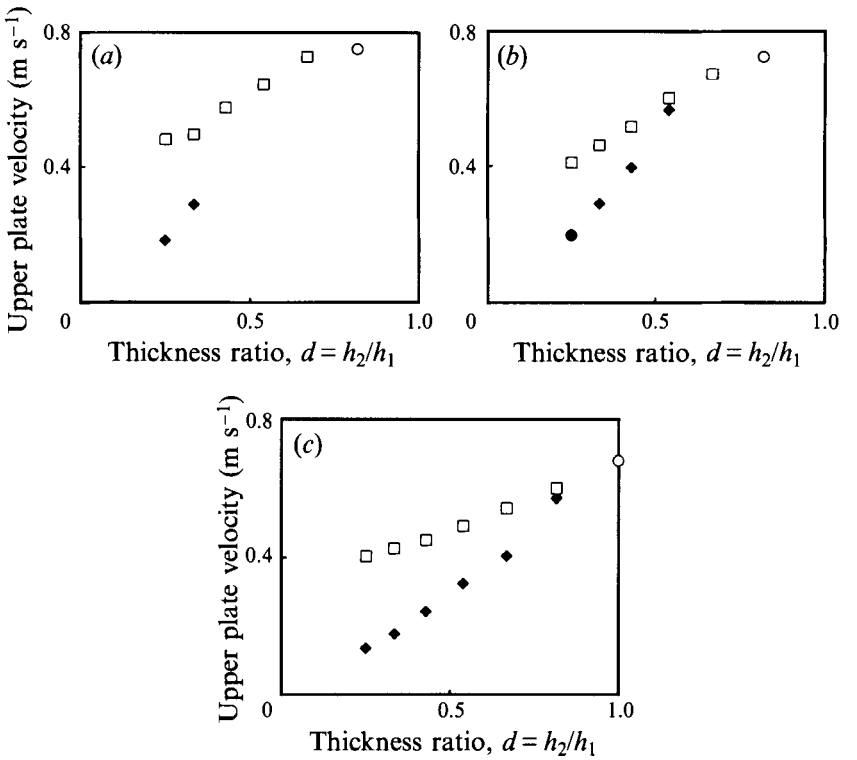

FIGURE 8. Critical velocities versus thickness ratio for the long wave (◆), the short wave (□) and the subcritical long wave (○), for viscosity ratio m = 1.55, 2.45 and 2.76 (*a–c*).

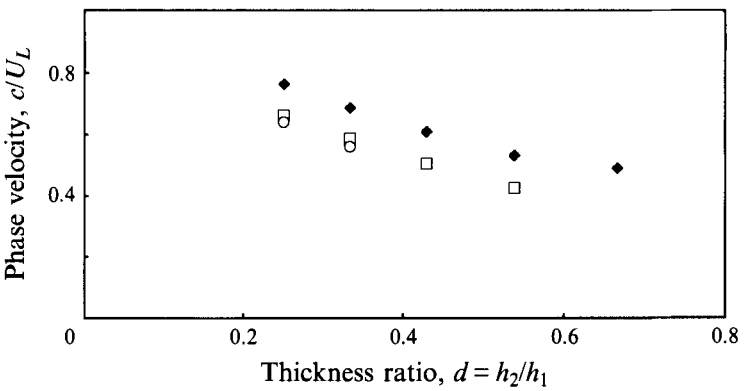

FIGURE 9. Dimensionless long-wave velocity c/U_L versus thickness ratio, for viscosity ratio m = 1.55 (○), 2.45 (□) and 2.76 (◆).

Reynolds, Froude or Weber numbers. For $R_0(m, d, r) > 0$, the flow is unstable owing to viscous stratification however small the Reynolds number. This viscous instability may be overcome by the stabilizing effect of gravity when the densities are not equal. Nevertheless, (4*b*) shows that this viscous instability can always be driven out for Froude number greater than

$$Fr_c = \frac{S}{R_0}\left\{1 + \frac{k^2}{Bo}\right\}, \tag{5}$$

	Couette flow	Cubic profile	Experiments
U_L (m s^{-1})	0.76	0.50	0.29

TABLE 2. Comparison of the theoretical critical velocities U_L to the experimental one, for fluids (1c–2) with thickness ratio $d = 0.33$

where $Bo \equiv We/Fr = \rho g h_1^2/\sigma$ is the Bond number. From (5) and from the definition of the Froude number, the critical velocity for a given flow can easily be obtained. Equation (5) also shows that long waves are destabilized first, which explains why the observed long wave has wavelength equal to the perimeter of the channel, which is its maximum allowed length.

However, the experimental value for the critical velocity is three or four times smaller than the theoretical one for plane Couette flow obtained from (5). Thus, the theoretical marginal stability curves have not been included in figure 8, since they are well above the experimental points. This discrepancy may be because the corresponding Reynolds number Re_1 is between 200 and 600. First, for such values of the Reynolds number, the flow is far from plane Couette flow, with a secondary flow and an inflexion point in the vertical profile of the azimuthal velocity. Secondly, Yih's solution may be no longer valid, since it assumes $Re = O(1)$.

To clarify this point, and following Yih (1967), the Orr–Sommerfeld equations have been solved for long waves with one experimental velocity profile measured just below the critical velocity U_L. This profile has been fitted accurately with a cubic polynomial in the lower fluid, keeping a linear profile in the upper layer. The velocity profile has been assumed self-similar as the upper plate velocity is varied, and the second flow has been ignored.

With such a cubic velocity profile, the critical upper plate velocity is lower than for Couette flow, but remains 75% above the experimental one, as shown in table 2. Since the eigenfunctions are the same, the nature of this long-wave interfacial instability is the same for both flows. The remaining discrepancy between critical velocities is probably due to tridimensional effects like the radial gradient of azimuthal velocity and secondary flow.

Finally, even if such a discrepancy between the theoretical predictions and the experimental results remains, the observed long-wave interfacial instability seems to correspond well to that found by Yih.

4. Saturated long waves

Figure 10 shows the saturated amplitude A_{sat} of the long wave, defined as half the crest-to-trough distance, versus upper plate velocity. The saturated amplitudes have been determined for increasing and then decreasing velocities.

Figure 10(a) corresponds to the supercritical case, the amplitude varying continuously as the upper plate velocity crosses its critical value, without any hysteresis. The power law can be determined from a log–log plot, and the critical exponent is found to be 1/2:

$$A_{sat} \sim (U - U_L)^{1/2}. \tag{6}$$

The saturated amplitude departs from the osculating parabola for $U \sim 1.4 U_L$ with amplitudes smaller than predicted by the above power law, and remains smaller than 1 mm.

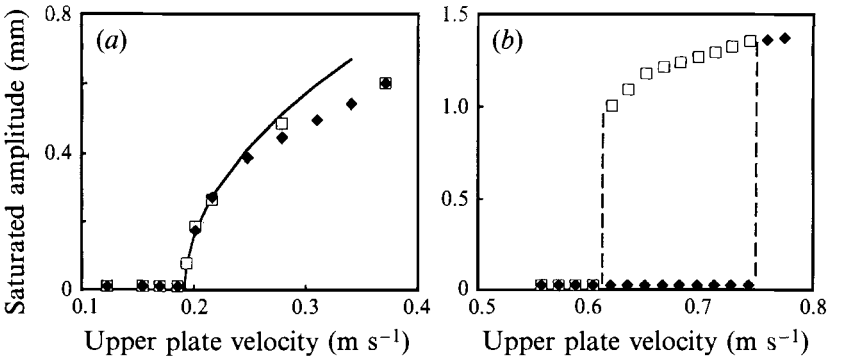

FIGURE 10. Amplitude of the saturated wave versus upper plate velocity, for increasing (◆) and decreasing velocity (□). (*a*) Supercritical long wave, fluids (1d–2), $d = 0.33$; ——, osculating parabola. (*b*) Subcritical long wave, fluids (1b–2), $d = 0.82$.

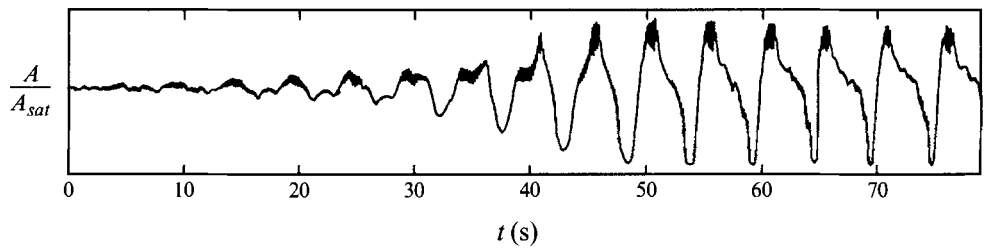

FIGURE 11. Rapid growth of the subcritical long wave, fluids (1b–2), $d = 0.82$, $U = 0.74$ m/s.

Figure 10(*b*) corresponds to the subcritical case. As the critical upper plate velocity is reached, the long wave suddenly appears, growing very quickly and reaching an amplitude greater than 1 mm. Figure 11 shows such an explosive growth. The amplitude grows slightly as the velocity is increased further, whereas the wave persists after the velocity is decreased below its critical value. This hysteresis and the finite jump of the amplitude at the threshold are characteristics of subcritical instabilities.

The rest of this paper is focused on the supercritical long wave. Figure 12 shows the evolution of the wave shape and the corresponding frequency spectra, as the velocity is increased beyond the onset of instability (amplitudes are normalized with the saturated amplitude for $U/U_L = 1.77$). Just above the onset of instability, the long wave appears sinusoidal (see also figure 7). Then the wave shape distorts rapidly, with steep fronts and sharp troughs, corresponding to the growth of harmonics. Moreover, the frequency spectra, plotted on a semi-logarithmic scale, show that near the onset of instability, the vertices of the peaks are aligned. This means that the amplitude A_n of the nth harmonic is proportional to A_1^n:

$$A_n \sim A_1^n. \tag{7}$$

This usual assumption in perturbation methods and 'weakly nonlinear' wave theory is known to be valid near the onset of instability, and its domain of validity corresponds roughly to that of the power law given by (6). Beyond the limit $U \sim 1.4U_L$, the amplitudes of the harmonics are higher than predicted by the above relation.

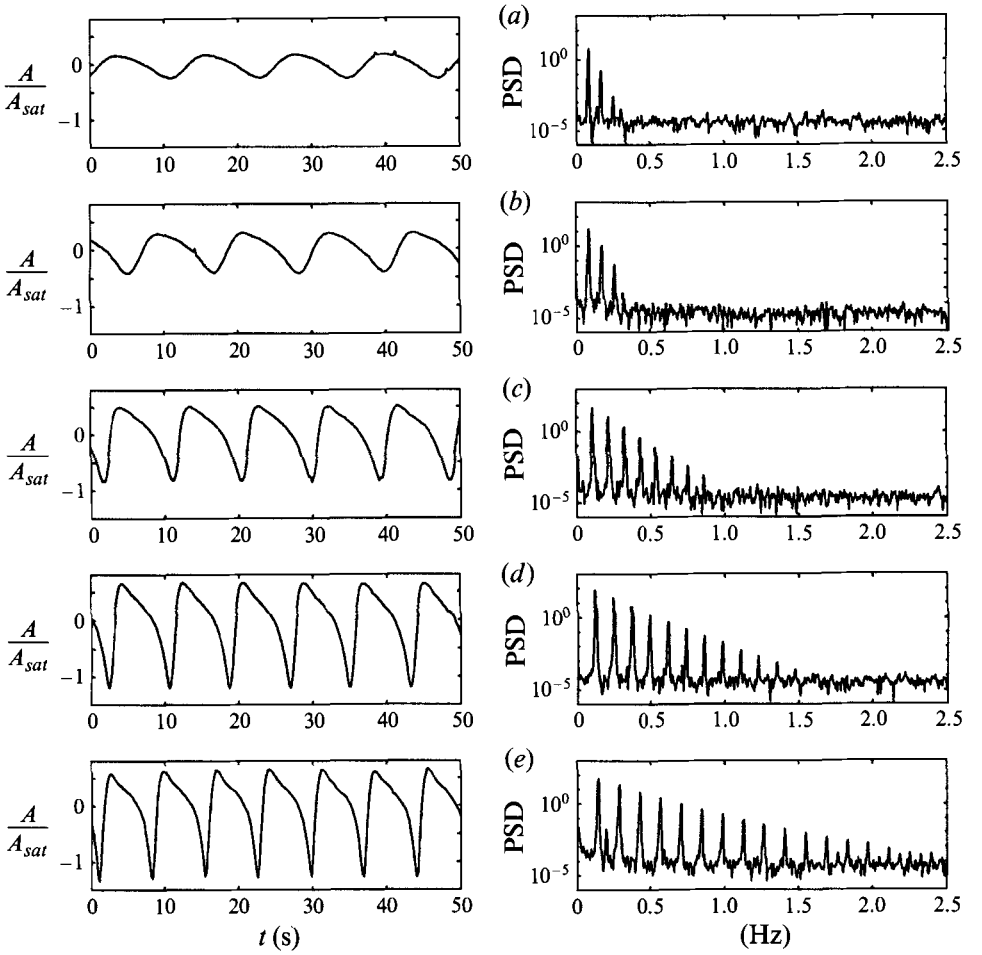

FIGURE 12. Time evolution of the interface position and frequency spectrum for the long wave, for $U/U_L = 1.06, 1.13, 1.33, 1.58$ and 1.77 (*a–e*). Amplitudes are normalized with the saturated amplitude for $U/U_L = 1.77$. Fluids (1d–2), $d = 0.25$, $U_L = 0.138$ m s^{-1}.

5. Transients of the supercritical long wave

5.1. *Spectrum evolution during the growth of the wave*

The preceding subsection showed that saturated waves involve an increasing number of harmonics as the velocity is increased beyond the threshold of instability. We now address the question of the growth of these harmonics, by considering the time evolution of the long wave from the flat interface up to saturation for fixed upper plate velocity $U > U_L$. This velocity is reached from rest in 10 s. The timescale for the basic flow to be established by viscous diffusion is about $0.25H^2/\nu$, where H is the total channel depth and ν is the kinematic viscosity of the less viscous fluid. This timescale is about 5 s. The timescale for the wave growth is much larger, so that one can consider that instabilities grow on a steady flow. As the recording starts, the basic flow is well established and instabilities have not yet reached a significant amplitude.

As shown in figure 13, the time for saturation τ is shorter with higher upper plate velocity, and follows the classical power law for critical phenomena:

$$\tau \sim (U - U_L)^{-1} \tag{8}$$

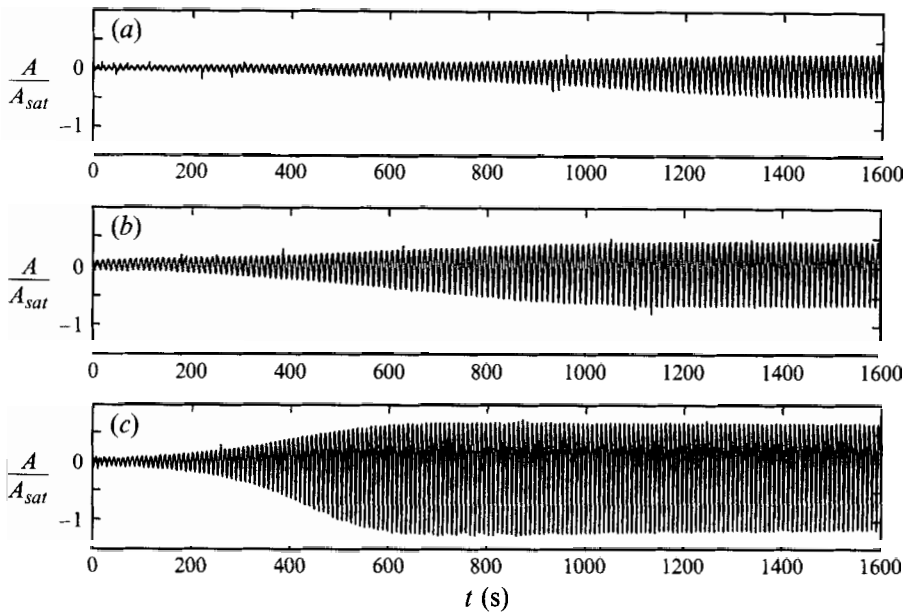

FIGURE 13. Long-wave growth for $U/U_L = 1.06$, 1.13 and 1.33 (*a–c*). Flow parameters: see figure 12.

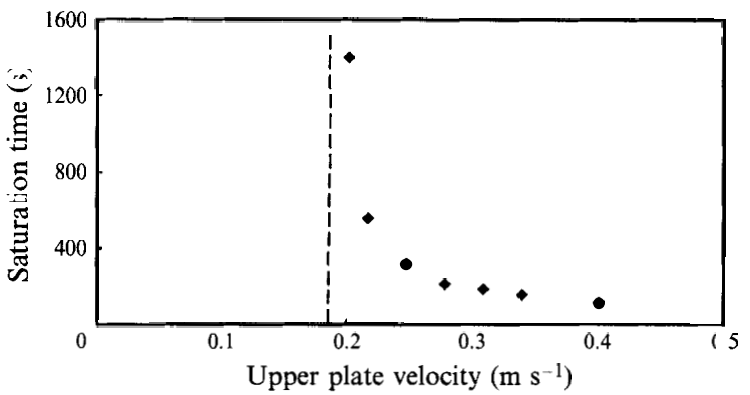

FIGURE 14. Saturation time τ for the long wave versus upper plate velocity. Fluids (1d–2), $d = 0.33$.

as the upper plate velocity U approaches its critical value U_L from higher values (figure 14). These very long transients allow detailed study of the growth of the harmonics. Figure 15 shows the evolution of the frequency spectrum with time, for fixed $U = 1.33U_L$. It can be seen that at the first stage of its growth, the long wave is dominated by its fundamental harmonic $k_1 = 2\pi/\pi D$, that harmonics grow as the amplitude increases, and that the spectrum stops evolving as soon as saturation is reached. More information can be obtained from the time records by reconstructing the amplitude and phase of each harmonic. The corresponding signal processing technique is described in the following subsection.

5.2. *Signal decomposition*

The problem is to obtain the amplitude and the phase of each harmonic of the interface position $\eta(x, t)$, from the signal recorded at the probe location $x = 0$. On the one hand,

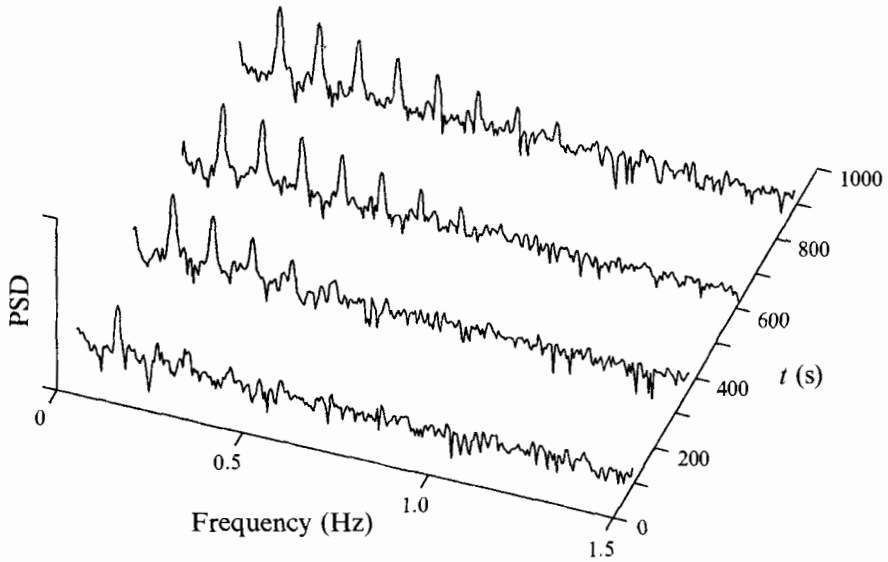

FIGURE 15. Evolution of the frequency spectrum with time, during the long-wave growth. The time evolution is the trace in figure 13(*c*).

spatial periodicity enables the interface position to be considered as the sum of its spatial Fourier components, each with wavenumber $k_n = nk_1$, where k_1 is the wavenumber of the fundamental harmonic. On the other hand, frequency spectra exhibit well-defined peaks (figure 15), with frequencies in multiples of the fundamental frequency, at the sampling accuracy. Thus, the interface position can be written as

$$\eta(x,t) = \frac{1}{2}\sum_{n=-\infty}^{\infty} A_n(t)\,\mathrm{e}^{\mathrm{i}n(\omega_1^0 t - k_1 x)} \quad \text{with} \quad A_{-n} = A_n^*, \tag{9}$$

where $A_n(t)$ is the complex amplitude of the nth spatial harmonic, and where $\omega_1^0 \equiv \omega(k_1, t \to 0)$ is the angular frequency of the fundamental harmonic at the first stage of its growth, or 'linear angular frequency'.

It must be stressed that, if the wavenumber $k_n = nk_1$ is the actual wavenumber of the nth harmonic, the frequency $n\omega_1^0$ cannot be considered as its actual frequency ω_n. The actual frequency may vary a little, owing to possible small dispersive effects (see (4)) or finite-amplitude effects as the amplitude grows. (This small frequency shift may not be identified in the spectra owing to the time averaging involved in the Fourier transform.) The slow variation $\phi_n(t)$ of the phase corresponding to this small frequency shift is taken into account in the complex amplitude. Thus the amplitude $A_n(t)$ is

$$A_n(t) = |A_n(t)|\,\mathrm{e}^{\mathrm{i}\phi_n(t)}. \tag{10}$$

Placing the origin of the x-axis at the probe location, the measured interface position is

$$\eta(0,t) = \frac{1}{2}\sum_{n=\infty}^{\infty} A_n(t)\,\mathrm{e}^{\mathrm{i}n\omega_1^0 t}. \tag{11}$$

Thus, the instantaneous phase $\Phi_n(t)$ and angular frequency $\omega_n(t)$ of the nth harmonic are

$$\Phi_n(t) = n\omega_1^0 t + \phi_n(t), \quad \omega_n(t) = n\omega_1^0 + \mathrm{d}\phi_n/\mathrm{d}t. \tag{12a, b}$$

The first step of the signal processing is to extract from the time record $\eta(0,t)$ the contribution $\eta_n(t)$ of the nth harmonic. This is achieved by band-pass filtering centred on $n\omega_1^0$ with a bandwidth equal to $\pm 0.2\omega_1^0$, and using a fourth-order Chebyshev filter. In order to keep the same time origin for all the harmonics, any phase distortion is cancelled by processing the signal for increasing and decreasing time. The contribution $\eta_n(t)$ is related to the complex amplitude by

$$\eta_n(t) = \tfrac{1}{2}\{A_n(t)\,\mathrm{e}^{\mathrm{i}n\omega_1^0 t} + \text{c.c.}\} = |A_n(t)|\cos\Phi_n(t). \tag{13}$$

Note that any non-zero amplitude A_0 can arise from centrifugal effects only, which give a conical shape to the interface and can change, at a fixed radius, the mean thickness of the fluids.

The second step of the signal processing is to recover the complex amplitude $A_n(t)$ from the real $\eta_n(t)$, i.e. to reconstruct the imaginary part of $A_n(t)$. The latter can be obtained from the Hilbert transform of $\eta_n(t)$, whose effect is to shift by $\pi/2$ the instantaneous phase of $\eta_n(t)$. The Hilbert transform $\mathrm{TH}[\eta_n(t)]$ is defined by (Melville 1983):

$$\mathrm{TH}[\eta_n(t)] = -\frac{1}{\pi t} * \eta_n(t) = \mathrm{TF}^{-1}[-\mathrm{i}\,\mathrm{sgn}(\nu)\,\mathrm{TF}[\eta_n(t)](\nu)], \tag{14}$$

where TF is the Fourier transform and where $*$ is the convolution operator. Thus, the complex amplitude is recovered as

$$A_n(t)\,\mathrm{e}^{\mathrm{i}n\omega_1^0 t} = \eta_n(t) + \mathrm{i}\,\mathrm{TH}[\eta_n(t)], \tag{15}$$

whose modulus and argument give the amplitude $|A_n(t)|$ and phase $\Phi_n(t)$ of the harmonic.

The first 30 s of each record have been discarded in order to avoid end effects due to filtering. We have verified that these techniques give pertinent results for quasi-monochromatic waves, whenever the timescale for the modulations is greater than three times the period of the wave. Before presenting the experimental results, we first turn to the theoretical predictions.

5.3. *Amplitude equations – the Landau–Stuart equation*

All the results presented in this subsection are dimensionless, with the lower layer thickness h_1 and the interface velocity U_I as characteristic scales. Long nonlinear interfacial waves $\eta(x,t)$ in Couette–Poiseuille flow have been studied by Hooper & Grimshaw (1985) within the framework of the Kuramoto–Sivashinsky equation. This equation is derived under the assumptions $Re = O(1)$ and $We = O(k^2)$ where k is the small dimensionless wavenumber (high surface tension). Charru & Fabre (1994) computed the next order in the small parameter k, allowing a less restrictive condition for the Weber number, namely $We = O(k)$. This next order introduces a linear dispersion term as well as other nonlinear terms of the same order. For amplitudes $O(k)$, this equation is

$$\eta_{,t} + \left\{ c_0\eta + \eta^2(V + \eta W) + Re_1(R + \eta T)\,\eta_{,x} + M\eta_{,xx} + \frac{Re_1 S}{We}\,\eta_{,xxx} \right\}_{,x} = 0, \tag{16}$$

where the coefficients of the linear terms, c_0, R, M and S, have been introduced in §3.3. The coefficients V and W are functions of the parameters m and d, and T depends, like R, on m, d, r and Fr.

The assumptions $Re = O(1)$ and $We = O(k)$ leading to the above equation are not

satisfied in our experiments, for which $Re = O(100)$ and $We = O(1)$. Nevertheless, here we consider (16) as a model equation for long waves, one that takes into account dissipative and dispersive effects, as well as the stabilizing effect of surface tension.

Searching for spatially periodic solutions, the interface can be developed in Fourier series (equation (9)). Inserting this expansion into the above interface equation, an infinite system of ordinary differential equations can be derived for the amplitudes $A_n(t)$:

$$\frac{\mathrm{d}A_n}{\mathrm{d}t} = (\sigma_n - \mathrm{i}n(n^2-1)\,\delta)\,A_n + (\mathrm{i}\alpha + n\beta)\sum_{p=-\infty}^{+\infty} pA_p\,A_{n-p} + \mathrm{i}\chi\sum_{p,q=-\infty}^{+\infty} pA_p\,A_q\,A_{n-p-q}, \tag{17a}$$

with

$$\alpha = k_1 V; \quad \beta = \tfrac{1}{2}k_1^2 Re_1\, T; \quad \delta = k_1^3 M; \quad \chi = \tfrac{3}{4}\mathrm{i}k_1 W, \tag{17b}$$

where the linear angular frequency $\omega_1^0 = \omega(k_1)$ and the growth rate $\sigma_n = \sigma(k_n)$ are defined by (4). Note that the δ-term corrects for the linear frequency $n\omega_1^0$, which arises from the dispersive term in the wave equation.

By keeping the first three harmonics, the following amplitude equations can be derived:

$$\frac{\mathrm{d}A_1}{\mathrm{d}t} = \sigma_1 A_1 + (\mathrm{i}\alpha+\beta)\,A_1^* A_2 + \mathrm{i}\chi A_1^2 A_1^* + k_1\,O(A_1^5), \tag{18a}$$

$$\frac{\mathrm{d}A_2}{\mathrm{d}t} = (\sigma_2 - 6\,\mathrm{i}\delta)\,A_2 + (\mathrm{i}\alpha+2\beta)\,A_1^2 + k_1\,O(A_1^4), \tag{18b}$$

$$\frac{\mathrm{d}A_3}{\mathrm{d}t} = (\sigma_3 - 24\mathrm{i}\delta)\,A_3 + 3(\mathrm{i}\alpha+3\beta)\,A_1 A_2 + \mathrm{i}\chi A_1^3 + k_1\,O(A_1^5). \tag{18c}$$

This dynamical system drives the time evolution of the complex 'generalized coordinates' A_i. This system can be greatly simplified near criticality, where the fundamental mode is the only unstable mode, while the others are linearly strongly damped:

$$\sigma_1 > 0, \quad \sigma_n < 0 \quad \text{with} \quad |\sigma_n| \gg \sigma_1 \quad \text{for} \quad n \geqslant 2. \tag{19}$$

Then the dynamics is controlled by the marginally unstable mode, to which the other modes are 'slaved' (Manneville 1990; Newell, Passot & Lega 1994). The arguments supporting this description are briefly outlined below.

Linear stability results show that, as the upper plate velocity is increased, the first unstable wave is the longest one, here with wavenumber k_1, for the Froude number $Fr_c(k_1)$ given by (5). As long as the Froude number is such that $Fr_c(k_1) \leqslant Fr < Fr_c(2k_1)$, the fundamental mode remains the only unstable one. According to (19), the timescale σ_1^{-1} for the growth of the fundamental is much greater than the relaxation times $|\sigma_n^{-1}|$ of the other harmonics, so that

$$\frac{\mathrm{d}A_n}{\mathrm{d}t} \sim \sigma_1 A_n \ll |\sigma_n|\,A_n \quad \text{for} \quad n \geqslant 2. \tag{20}$$

Thus, from (18), the dynamics of the harmonics is 'slaved' to the dynamics of the fundamental harmonic, according to

$$A_2 = -\frac{\mathrm{i}\alpha+2\beta}{\sigma_2 - 6\mathrm{i}\delta}A_1^2 + k_1\,O(A_1^4) \tag{21a}$$

for A_2, and similarly for A_3:

$$A_3 \sim A_1^3 + k_1 O(A_1^5). \tag{21b}$$

From these relations, it follows that the amplitude and phase of each harmonic is linked to those of the fundamental harmonic through the relations

$$|A_n| = \text{const.}\,|A_1|^n \quad \text{and} \quad \phi_n(t) = n\phi_1(t) + \text{const.} \tag{22}$$

Thus, although the harmonics are linearly stable ($\sigma_n < 0$), they grow through nonlinear interactions, with energy supplied by the fundamental harmonic. Their actual growth rate satisfies

$$\frac{1}{|A_n|}\frac{\mathrm{d}|A_n|}{\mathrm{d}t} = n\frac{1}{|A_1|}\frac{\mathrm{d}|A_1|}{\mathrm{d}t} = n\sigma_1. \tag{23}$$

The dynamics of the system is governed by the marginally unstable fundamental harmonic. From (21*a*) and (18*a*), this fundamental harmonic obeys the Landau–Stuart equation

$$\frac{\mathrm{d}A_1}{\mathrm{d}t} = \sigma_1 A_1 - \kappa A_1^2 A_1^* + k_1 O(A_1^5), \tag{24}$$

where κ is the complex Landau–Stuart constant whose explicit expression can be easily obtained. Its real part κ_r corresponds to nonlinear dissipation, and its imaginary part κ_i to nonlinear frequency correction. The Kuramoto–Sivashinsky truncation of (16) (obtained for $W = T = M = 0$) leads to a real positive Landau–Stuart constant, corresponding to supercritical instability without any nonlinear frequency variation. On the other hand, considering the complete (16), the real part κ_r of the Landau–Stuart constant could be negative, for example for $\delta = 0$ and $\alpha^2 < 2\beta^2$, i.e. $M = 0$ and $2V^2 < k_1^2 Re_1^2 T^2$. Strictly speaking, this relation violates the assumptions under which (16) is derived ($k_1 \ll 1$, $V \sim T \sim Re_1 \sim 1$), but it could account for the subcritical instability reported here (figure 10*b*).

The Landau–Stuart equation has already been obtained by Renardy (1989) from the point of view of the central manifold theorem, using numerically computed eigenvalues and eigenfunctions. Unfortunately, Renardy's values of κ correspond to wavenumbers greater than unity, and cannot be compared with long-wave predictions.

5.4. *Harmonics evolution near the onset of instability*

Near the onset of instability, and for given flow conditions (same fluids, same upper plate velocity), each run exhibits the same transient and leads to the same periodic saturated wave. Figure 16 displays the experimental behaviour of the harmonics for upper plate velocity $U = 1.13U_L$. The time evolution is drawn in figure 16(*a*): the wave grows and saturates after about 1200 s. The period at saturation is $T_{sat} = 11.1$ s.

The time evolutions of the amplitudes of the first three harmonics are depicted in figure 16(*b*) (time is normalized with the period at saturation T_{sat}). At the outset the wave is monochromatic. Harmonics then successively emerge, and simultaneously reach saturation. A more accurate view can be gained with a logarithmic plot of the amplitudes. Figure 16(*d*) clearly displays, for each harmonic, three distinct stages: an exponential growth, a transition stage and a saturation stage. As predicted by the theoretical analysis, (22), the amplitude ratios $|A_n|/|A_1|^n$ remain constant from the birth of the harmonics up to saturation (figure 16*e*).

The time evolution of the phases $\Phi_n(t)$, defined by (12*a*), is plotted in figure 16(*c*). They are nearly linear, with slope proportional to the order n of the harmonic. This

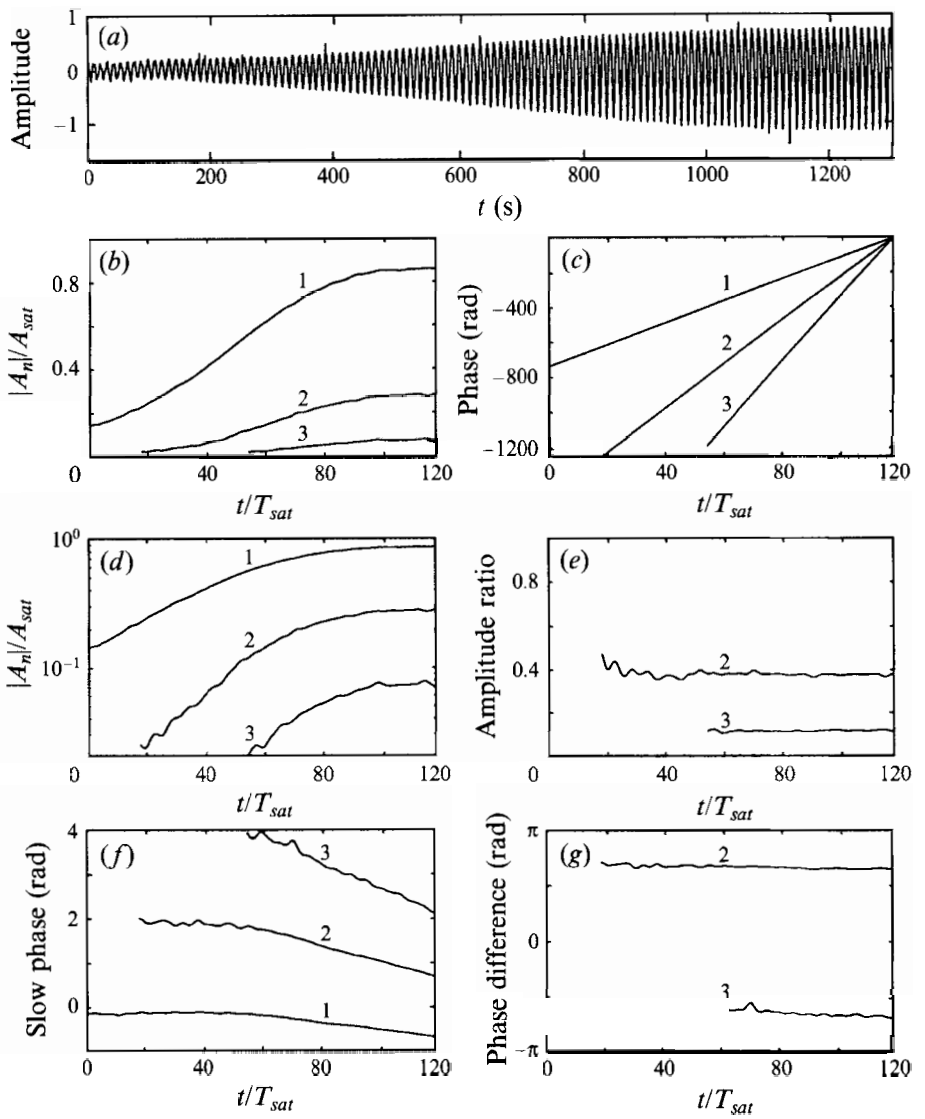

FIGURE 16. Evolution of the interface for $U/U_L = 1.13$. (*a*) Time evolution. (*b*) Amplitudes $|A_n|/A_{sat}$ of the first three harmonics. (*c*) Phases Φ_n. (*d*) Log$|A_n|/A_{sat}$. (*e*) Ratios $\{|A_n|/A_{sat}\}/\{|A_1|/A_{sat}\}^n$. (*f*) Slowly varying phases ϕ_n. (*g*) Phase differences $\phi_n - n\phi_1$. Flow parameters: see figure 12. $T_{sat} = 11.1$ s.

linear behaviour supports the aforementioned decomposition of the phase into one rapidly varying term $n\omega_1^0 t$, where ω_1^0 is the linear angular frequency of the fundamental harmonic, and one slowly varying term $\phi_n(t)$.

The deviation from linearity can be magnified by subtracting from the phase $\Phi_n(t)$ its rapidly varying part $n\omega_1^0 t$, in order to reveal the slow phase $\phi_n(t)$ (figure 16*f*). The frequency ω_1^0 of the fundamental harmonic has been determined as

$$\omega_1^0 \equiv \omega(k_1, t \to 0) \tag{25}$$

by linear fitting of the phase $\Phi_1(t)$ in the exponential growth stage by a least-squares method. As for the amplitude, the time evolution of the slow phase $\phi_n(t)$ exhibits three

$\omega_2^\infty/\omega_1^\infty$	$\omega_3^\infty/\omega_1^\infty$	$\omega_1^\infty/\omega_1^0$
2.000	3.000	0.998

TABLE 3. Frequency ratios for $U = 1.13U_L$

stages, at least for the first two harmonics. In the exponential stage, $\phi_1(t)$ and $\phi_2(t)$ remain constant, whereas $\phi_3(t)$ is not defined since A_3 has not yet emerged. Thus, according to (12*b*), the frequency of the second harmonic is twice the fundamental harmonic one. In the transition stage, the slow phases decrease; their time derivatives decrease as well, corresponding to decreasing wave frequencies. In the saturation stage, the $\phi_n(t)$ decrease with constant slope proportional to the order of the harmonic: this means that the frequencies at saturation, determined as

$$\omega_n^\infty \equiv \omega(k_n, t \to \infty), \tag{26}$$

are locked to multiples of the fundamental frequency (table 3). The frequency shift is about 0.2% between the exponential growth and saturation stages.

These observations are made clearer by plotting of the phase differences (figure 16*g*)

$$\Phi_n(t) - n\Phi_1(t) = \phi_n(t) - n\phi_1(t), \quad n = 2, 3 \tag{27}$$

that compare the phase of the harmonics to the fundamental one. These phase differences can be seen as the relative spatial position of the nth harmonic with respect to the fundamental. They appear to remain constant from the birth of the harmonics up to saturation, as predicted by theoretical analysis, (22). They are close to $3\pi/4$ for $n = 2$, and close to $-\pi/2$ for $n = 3$.

Finally, for $U = 1.13U_L$, the complex amplitudes A_2 and A_3 are proportional to A_1^2 and A_1^3 respectively, as shown by the constant values of amplitude ratios (figure 16*e*) and phase differences (figure 16*g*): the validity of the analysis in terms of central and slaved modes is thus confirmed.

As the upper plate velocity is increased further, the amplitude of the wave, and consequently that of the harmonics, increases. Figure 17 shows the time evolution of the amplitude and phases of the first three harmonics for upper plate velocity $U = 1.33U_L$. These evolutions are qualitatively the same as for $U = 1.13U_L$. The time evolution is presented in figure 17(*a*). The logarithmic plot of the amplitudes (figure 17*b*) shows the monochromatic character of the wave in the early stages of its growth. The plot of the amplitude ratios $|A_n|/|A_1|^n$ shows that these ratios remain constant as soon as the harmonics emerge (figure 17*c*).

The slowly varying phase $\phi_n(t)$ exhibits qualitatively the same behaviour as for $U = 1.13U_L$ (figure 17*d*). Nevertheless, it appears that during the growth period, phase differences are no longer constant and decrease very slowly (figure 17*e*). Since the phase difference is related to the relative wave velocity $c_n - c_1$ through

$$c_n - c_1 = \frac{\omega_n}{nk_1} - \frac{\omega_1}{k_1} = \frac{1}{nk_1}\frac{\mathrm{d}}{\mathrm{d}t}\{\phi_n - n\phi_1\}, \tag{28}$$

the above decrease of the phase differences corresponds to small dispersive effects. Phase differences and amplitudes reach their saturation value simultaneously, and the frequencies are then locked. The values of the phase differences at saturation, which determine the wave shape, appear to be approximately the same as for $U = 1.13U_L$. The dispersive behaviour is the precursor of more complex ones, e.g. harmonics

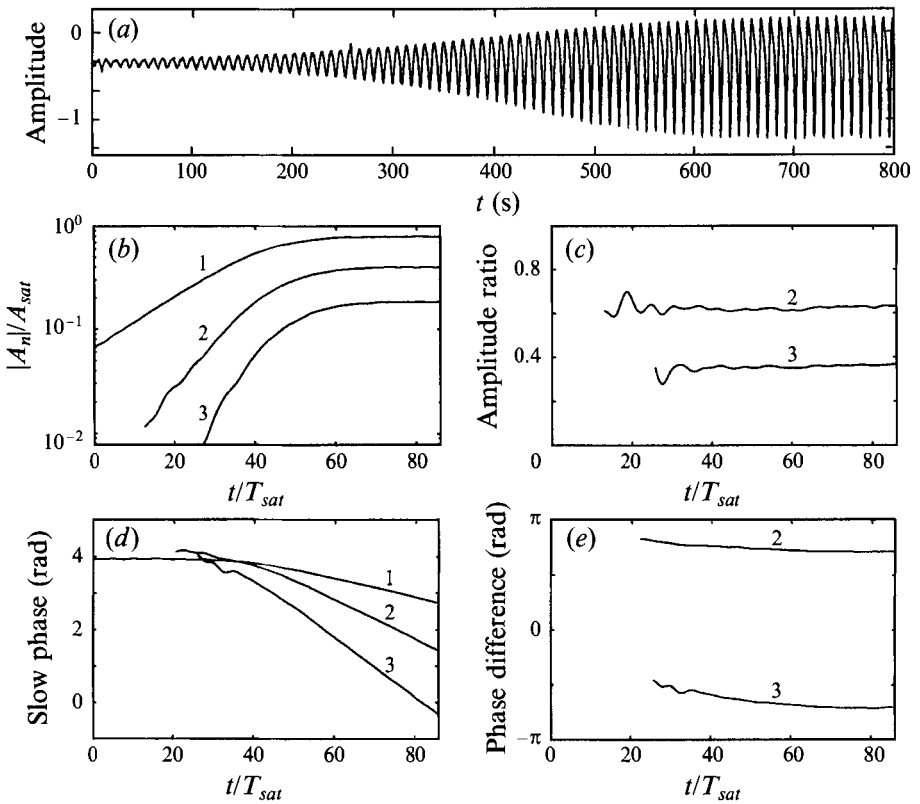

FIGURE 17. Evolution of the interface for $U/U_L = 1.33$. (*a*) Time evolution. (*b*) Amplitudes $|A_n|/A_{sat}$ of the first three harmonics. (*c*) Ratios $\{|A_n|/A_{sat}\}/\{|A_1|A_{sat}\}^n$. (*d*) Slowly varying phases ϕ_n. (*e*) Phase differences $\phi_n - n\phi_1$. Flow parameters: see figure 12. $T_{sat} = 9.4$ s.

U/U_L	σ_1 (10^{-3} s^{-1})	ω_1^0 (rad s^{-1})	κ_r (mm^{-2} s^{-1})	κ_i/κ_r
1.13	2.6	0.5677	0.0835	0.404
1.33	6.2	0.6748	0.0753	0.503

TABLE 4. Numerical values of the coefficients of the Landau–Stuart equation, computed from the least-squares method. κ_r is the only coefficient to be sensitive to the calibration of amplitude

gaining autonomy, and it shows the limits of an approach based on central and slaved modes.

As an ultimate confirmation of the validity of the model, the coefficients of the Landau–Stuart equation for the complex amplitude A_1 can now be determined. This can be achieved by computing numerically the time derivatives $\mathrm{d}|A_1|/\mathrm{d}t$ and $\mathrm{d}\phi_1/\mathrm{d}t$ from the time series of $|A_1|$ and ϕ_1, and then fitting the numerical coefficients of the Landau–Stuart equation using a least-squares method. With these coefficients (table 4), the numerical solution of the Landau–Stuart equation may be compared to the original time series for $|A_1|$ and ϕ_1. As expected, close agreement is found from the Landau–Stuart equation truncated to the cubic term: the numerical reconstruction exactly fits the traces of the amplitude $|A_1|$ and of the phase ϕ_1 shown in figures 16(*b*) and 16(*f*). As expected from the decrease of the slow phases in the nonlinear regime (figures 16*f* and 17*d*), the imaginary part of the Landau–Stuart constant is non-zero.

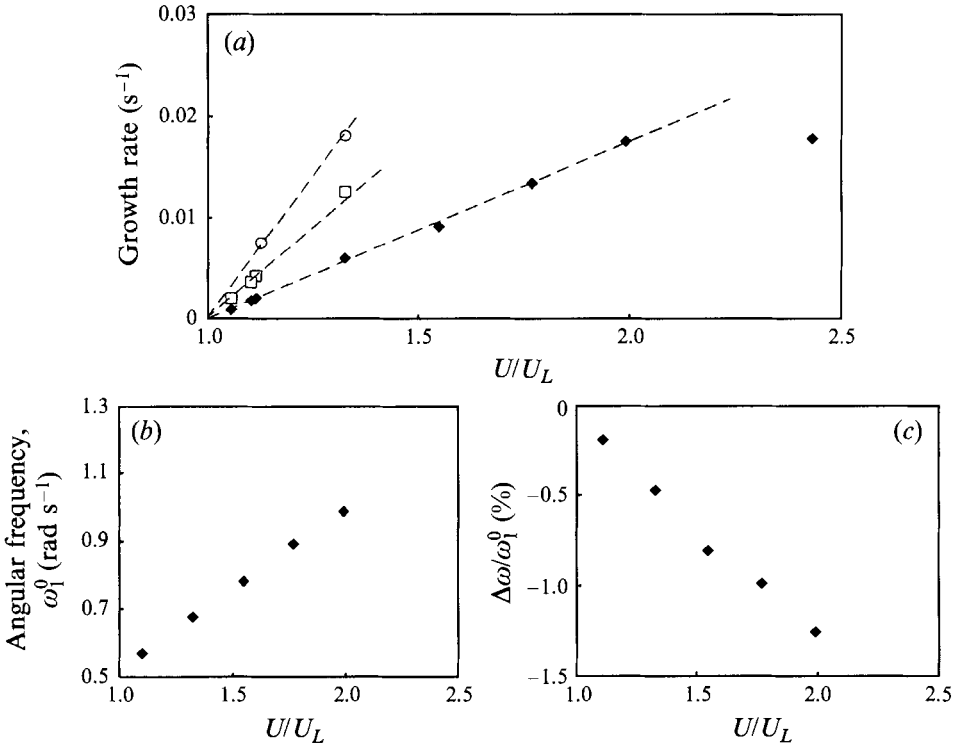

FIGURE 18. Evolution with upper plate velocity of (*a*) the growth rate of the harmonics; (*b*) the fundamental linear frequency ω_1^0; (*c*) the fundamental frequency shift $(\omega_1^\infty - \omega_1^0)/\omega_1^0$.

Finally, it can be said that up to $U \approx 1.4U_L$, the experimental results qualitatively agree with all the aspects of the central and slaved modes analysis.

Figure 18 displays results for the growth rate and the frequency of the first three harmonics as the upper plate velocity is increased. The growth rates, presented in figure 18(*a*), were obtained by a linear fitting to $\log(|A_n|)$ in the exponential growth zone. The growth rate σ_1 of the fundamental harmonic remains very low, at most 2×10^{-2} s^{-1}. It is a linear function of the distance to the threshold, as predicted by the theory, but this linear behaviour still exists away from the threshold. Near the critical velocity, the growth rate of the nth harmonic is equal to $n\sigma_1$ according to (23). For higher velocities, these growth rates experience large variations during transients, and these variations differ from one run to another. This is why these growth rates are plotted for $U < 1.4U_L$ only, which appears to be the domain of validity of the central and slaved modes analysis.

The linear frequency ω_1^0 and the frequency shift $(\omega_1^\infty - \omega_1^0)/\omega_1^0$ of the fundamental harmonic are presented in figures 18(*b*) and 18(*c*) respectively. Like the growth rates, they exhibit a linear behaviour in a wide range of upper plate velocities. The frequency shift due to finite amplitude effects is always negative, corresponding to a decrease of the wave velocity from its birth up to saturation. It stays lower than 1.5% of the linear frequency.

5.5. *The rebellion of the slaved modes*

For an upper plate velocity higher than $1.4U_L$, each run of the experiment still leads to the same periodic wave for given flow conditions. However, a new phenomenon arises: the transient ceases to be unique, it differs from one run to another. This is

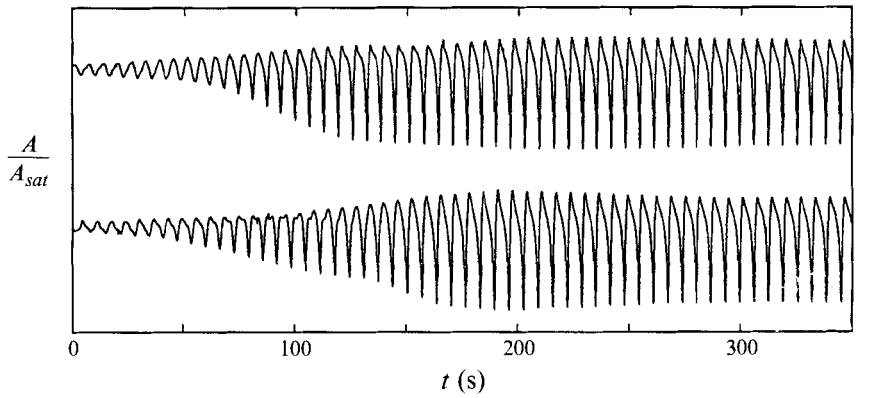

FIGURE 19. Two different transients for the same upper plate velocity $U = 2U_L$. Flow parameters: see figure 12.

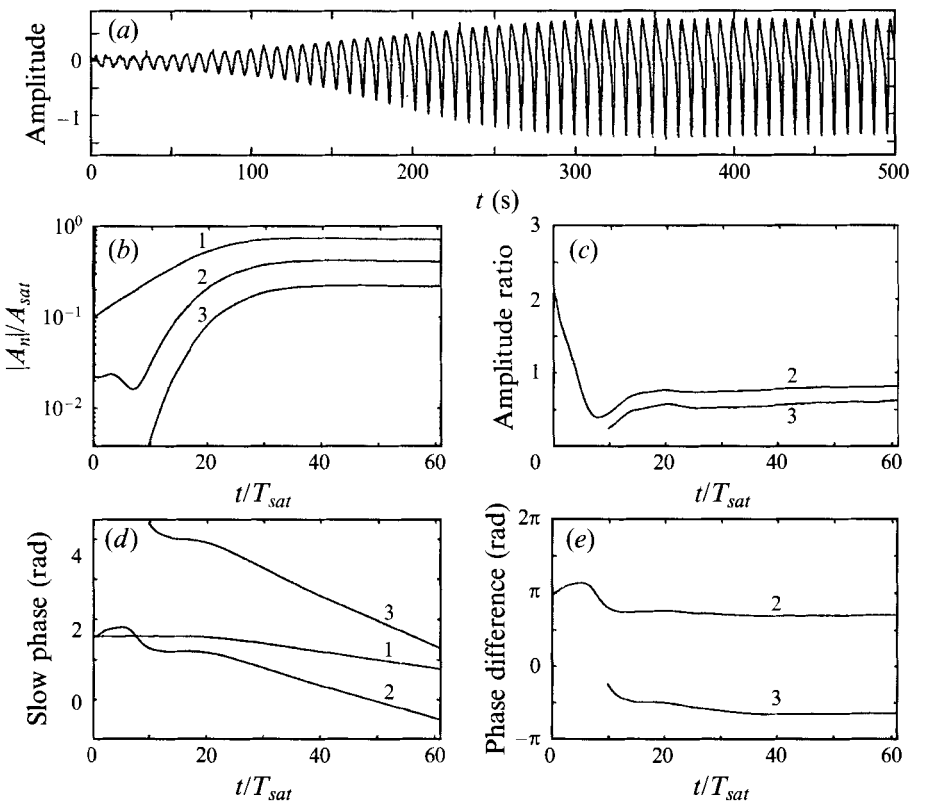

FIGURE 20. Time evolution of the interface, and amplitude and phase of the first three harmonics for $U/U_L = 1.58$. Flow parameters: see figure 12. $T_{sat} = 8.1$ s.

evident in figure 19, which shows two runs for $U = 2U_L$. Despite these different behaviours, these transients have in common an amazing feature: the growth of the harmonics is marked by sharp frequency locking between them, related to the collapse of their amplitude. This striking feature is illustrated by two examples.

Figure 20 displays the transient for $U = 1.58U_L$. The time evolution (figure 20*a*) looks qualitatively the same as for lower velocity. Nevertheless, closer observation

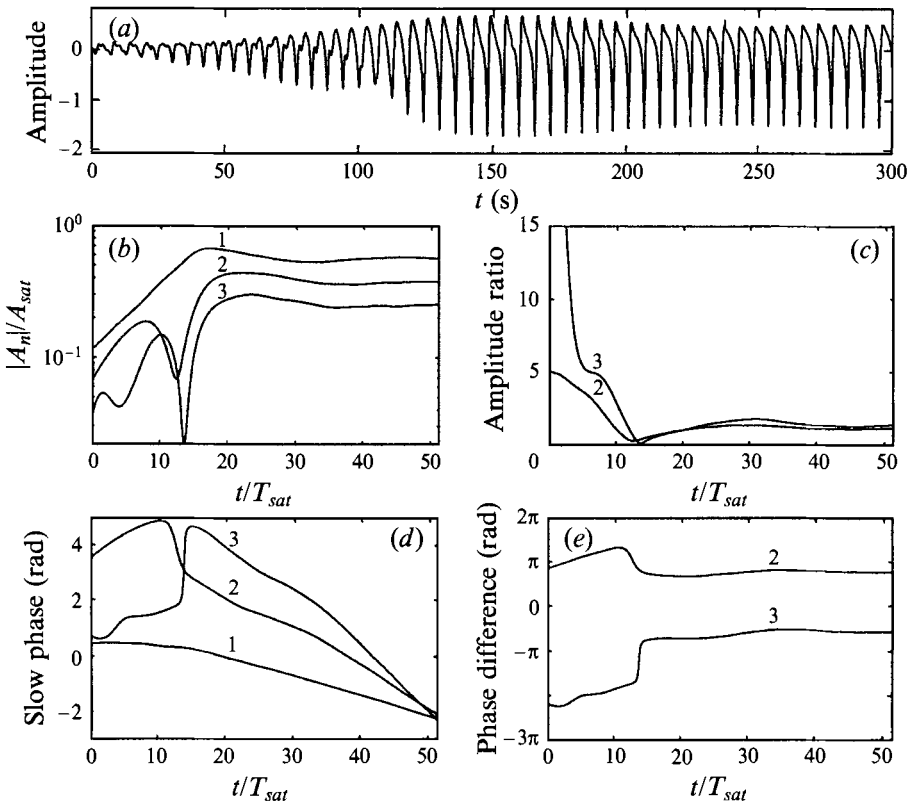

FIGURE 21. Time evolution of the interface, and amplitude and phase of the first three harmonics for $U/U_L = 2.25$. Flow parameters: see figure 12. $T_{sat} = 6.5$ s.

shows the existence of a little hump, sliding on the fundamental during the first growth stage. This hump corresponds to the emancipated second harmonic running faster than the fundamental, with amplitude much larger than previously (figure 20*b*). Whereas the fundamental harmonic A_1 grows smoothly, the second harmonic A_2 stops growing and even decreases, before growing again at a rate roughly three times faster than that of A_1. The amplitude ratios $|A_n|/|A_1|^n$ confirm clearly that the higher harmonics are no longer slaved to the fundamental (figure 20*c*).

The slow phases ϕ_n are shown in figure 20(*d*). Whereas ϕ_1 decreases without any accident, the slow phase ϕ_2 first increases, then sharply decreases and finally behaves as previously; ϕ_3 exhibits the same behaviour. The significance of these behaviours appears in the phase differences (figure 20*e*). According to (28), the velocity differences or frequency differences may be read as the slope of these curves. It appears that A_2 first travels faster than A_1, and then suddenly brakes when its amplitude is at a minimum, and adjusts its velocity to that of A_1. This velocity or frequency locking occurs very early, taking advantage of a propitious phase difference. On the other hand, A_3 not only follows A_1 as previously, but appears to be strongly influenced by the evolution of A_2. The phase differences at saturation keep approximately the same value that they had previously.

These behaviours are magnified as the upper plate velocity is increased further (figure 21, $U = 2.25U_L$). The time evolution (figure 21*a*) now shows more clearly the existence of a sliding hump at the beginning. Turning to the evolution of the harmonics

(figure 21 *b–e*), it appears that the fundamental harmonic grows exponentially as usual, ignoring the complicated stories of its small brothers, but suddenly saturates and then relaxes gradually to its saturation value. The second harmonic A_2 has qualitatively the same behaviour as previously. It travels with constant velocity 1.0% faster than A_1, until it collapses and brakes suddenly, locking its velocity to that of A_1. The third harmonic A_3 collapses twice. The first time, it adjusts its velocity to A_2, and the second time, to the common velocity of A_1 and A_2. The relative phase $\phi_2-2\phi_1$ experiences a jump of $-\pi/2$ concomitant with the collapse of A_2, and $\phi_3-3\phi_1$ experiences a jump of π concomitant with the second collapse of A_3.

The dispersive character of the waves plays a crucial role in the occurrence of these amplitude collapses and frequency locking. This may be understood within the framework of (18) after separation of modulus and phase of the complex amplitudes. The translational invariance of (16) implies that only phase differences are relevant. Thus, the equations for the moduli $|A_1|$ and $|A_2|$ and for the phase difference $\Delta\phi = \phi_2-2\phi_1$ are

$$\frac{\mathrm{d}|A_1|}{\mathrm{d}t} = \sigma_1|A_1| + |A_1||A_2|(\beta\cos\Delta\phi - \alpha\sin\Delta\phi), \tag{29a}$$

$$\frac{\mathrm{d}|A_2|}{\mathrm{d}t} = \sigma_2|A_2| + |A_1|^2(2\beta\cos\Delta\phi + \alpha\sin\Delta\phi), \tag{29b}$$

$$\frac{\mathrm{d}\Delta\phi}{\mathrm{d}t} = -6\delta - 2\chi|A_1|^2 - 2|A_2|(\alpha\cos\Delta\phi + \beta\sin\Delta\phi) + \frac{|A_1|^2}{|A_2|}(\alpha\cos\Delta\phi - 2\beta\sin\Delta\phi). \tag{29c}$$

The linear increase of $\Delta\phi$ shown on figure 21 (*e*) at the beginning of the growth can only come from the linear dispersive term δ in (29*c*). Such a variation of $\Delta\phi$ leads to the change of sign of the nonlinear term of (29*b*) and consequently to the damping of the second harmonic and its collapse. The last term in (29*c*) thus becomes very large, leading to the quick variation of $\Delta\phi$ shown on figure 21 (*e*). The subsequent frequency locking seems out of reach of a simple explanation, but it can be reproduced by numerical integration of (29).

Owing to the random character of the initial phases and amplitudes, the details of the occurrence of amplitude collapses and frequency locking may vary. This explains the variability of the transients from one run to another mentioned at the beginning of this subsection.

5.6. *The battle of the chiefs: bistability*

As the upper plate velocity is increased further ($U > 2.4U_L$), two different saturated waves can be observed for the same flow conditions, as shown on figure 22. The saturated wave is dominated either by the fundamental harmonic (one wavelength in the channel) or by the second harmonic (two wavelengths in the channel). This corresponds to bistability, the final state evidently depending on the random noise from which unstable modes emerge.

Transients leading to each wave are displayed in figures 23 and 24 ($U = 2.43U_L$). On the one hand, figure 23 shows the gentle growth of the five first harmonics, up to the saturated wave dominated by the fundamental harmonic (phase evolutions appear meaningless and have not been reported here). This evolution is just perturbed by the momentary collapse of A_2, which passes on each harmonic successively. On the other hand, figure 24 shows a different response: the fundamental harmonic first dominates, but then decays and finally vanishes, whereas the second eventually dominates after several oscillations. It seems that A_2 and A_3 have opposite growth rates, the one

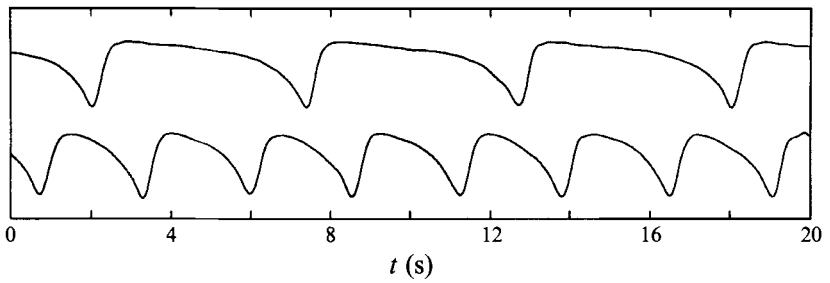

FIGURE 22. The two saturated waves for $U/U_L = 2.43$, dominated either by the fundamental harmonic or by the second harmonic. Flow parameters: see figure 12.

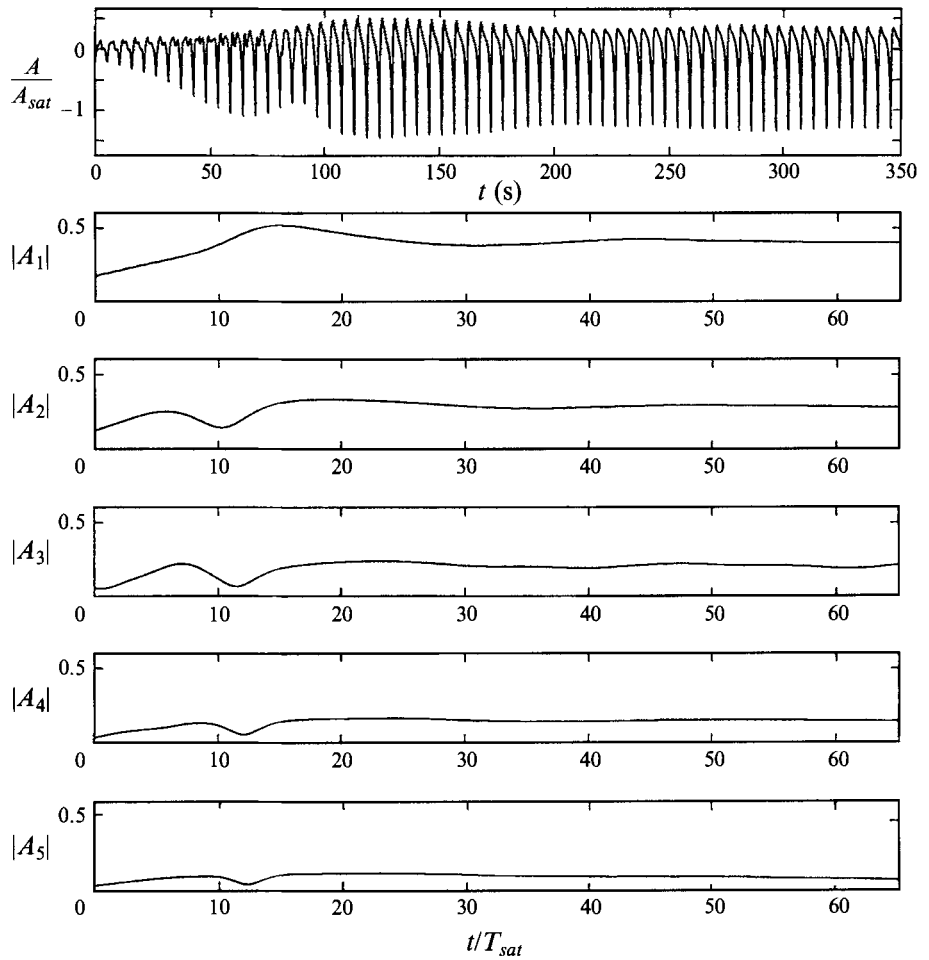

FIGURE 23. Time evolution of the interface, and amplitude of the first harmonics for $U/U_L = 2.43$. Flow parameters: see figure 12. The final state is dominated by the fundamental harmonic.

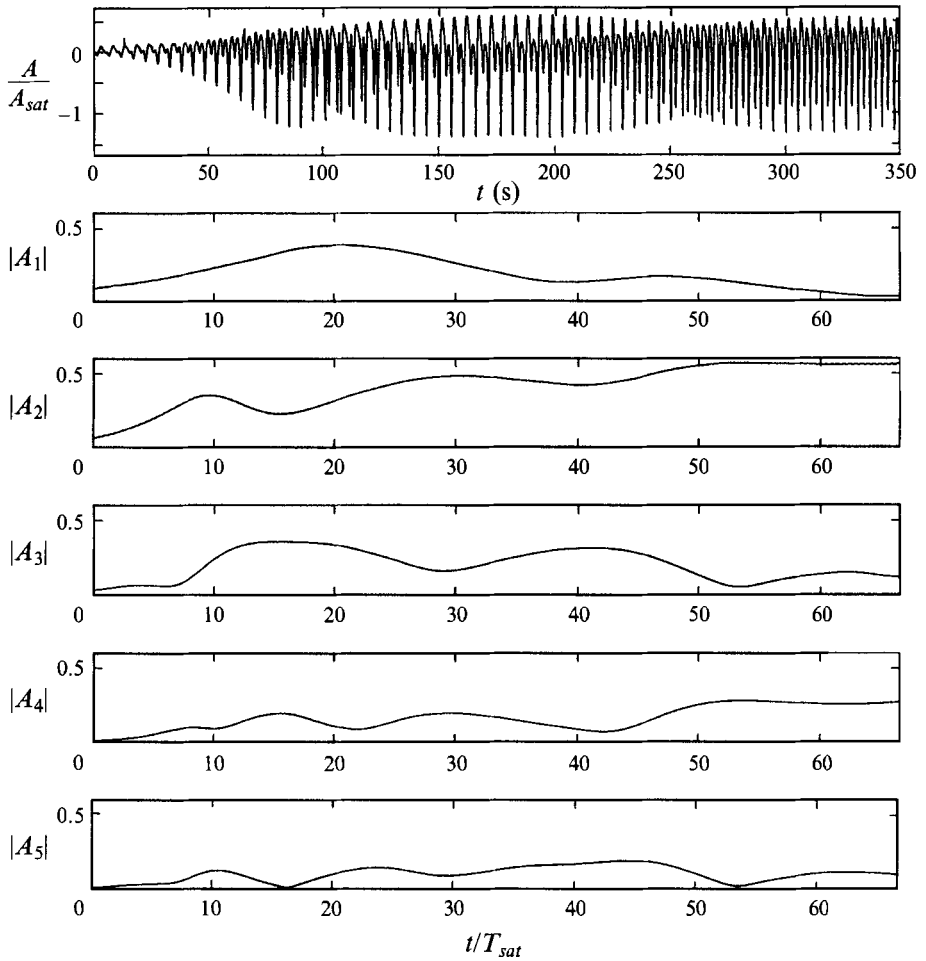

FIGURE 24. Time evolution of the interface, and amplitude of the five first harmonics for $U/U_L = 2.43$. Flow parameters: see figure 12. The final state is dominated by the second harmonic.

growing while the other decays, suggesting cyclic energy exchange between harmonics. The harmonics A_4 and A_5 display the same cyclic energy exchange. For the transient shown on figure 24, the saturated wave shown on figure 22 has not yet been reached.

6. Summary and discussion

Experimental results on the interfacial stability of two-layered Couette flow have been presented. Experiments were performed in a channel bent into an annular ring, so that the wavenumber spectrum was discrete and the wave evolution could be observed over very long times. Two kinds of interfacial waves were observed, depending on the viscosity ratio and thickness ratios: they correspond to long-wave instability and $k = O(1)$ instability. This paper is focused on the long-wave instability.

The long wave appears with wavelength equal to the perimeter of the channel, beyond some critical velocity U_L of the upper plate. The comparison with the long-wave stability analysis of Yih reveals that experimental critical velocities are roughly three times smaller than the predicted ones. However, the critical velocities correspond to Reynolds numbers of about 400, for which the basic flow departs from Couette flow

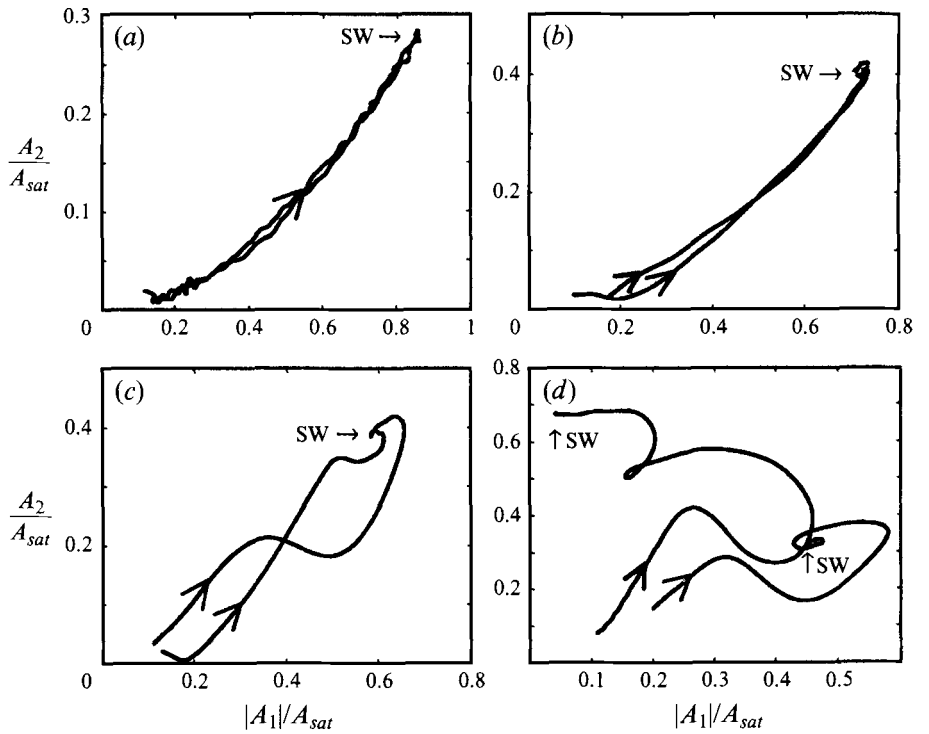

FIGURE 25. Phase portraits in the plane $(|A_1|, |A_2|)$. (*a*) $U/U_L = 1.13$; (*b*) $U/U_L = 1.58$; (*c*) $U/U_L = 2$; (*d*) $U/U_L = 12.43$. Each trace corresponds to one run. SW: saturated wave. Flow parameters: see figure 12.

owing to centrifugal effects. When the actual velocity profile is taken into account in the stability analysis, the overestimation is reduced to 75%. The remaining discrepancy is probably due to the destabilizing effect of the secondary flow.

The bifurcation is generally supercritical, but it is subcritical for thickness ratio close to unity. The critical exponents of the supercritical bifurcation have been calculated and they agree with the classical Landau theory.

The supercritical long wave arises from a soft instability, with a growth rate of about 10^{-3} s^{-1}, and original insight on the nonlinear wave dynamics was gained from the study of the long transients. The study was carried out within the theoretical framework of amplitude equations for confined systems, obtained from the long-wave interface equation derived by Charru & Fabre (1994). The amplitude and phase of each harmonic were accurately obtained by using the Hilbert transformation. The results are illustrated in terms of dynamical systems on figure 25, which shows the trajectories of the system projected onto the plane $(|A_1|, |A_2|)$, for various upper plate velocities. These plots allow the time to be eliminated and attention to be focused on the related dynamics of A_1 and A_2. For each upper plate velocity, two trajectories are plotted, corresponding to the same flow conditions.

Near the onset of instability, the fundamental harmonic is the only unstable one, and the time evolution of the harmonics closely follows the analysis in terms of central and slaved modes. Indeed, the fundamental follows the Landau–Stuart equation, and the amplitude ratios $|A_n|/|A_1|^n$ and the phase differences $\phi_n - n\phi_1$ remain constant during the growth up to saturation. These results are illustrated on figure 25(*a*). The two trajectories leading from the origin (flat interface) to the unique fixed point (saturated

wave) are merged. The trajectory is a parabola, according to the slaved mode theory. This parabola can be viewed as an experimental centre manifold which strongly attracts the random initial point, quickly enough for the different runs to be indistinguishable.

As the upper plate velocity is increased ($U > 1.4U_L$), the transients are more complicated and can vary significantly from one run to another, but they always lead to the same saturated wave for given flow conditions. The typical behaviour of these transients can be described as follows. At the beginning, the second harmonic first travels faster than the fundamental. The relative velocity has been shown to be constant during this stage, and corresponds to linear dispersion. Then the second harmonic suddenly brakes and adjusts its velocity to the fundamental, through a remarkable collapse of its amplitude and through a phase jump. Velocities and thus frequencies then remain locked. The third harmonic behaves similarly. Differences in the details of the transients are due to random initial amplitudes and phases of the harmonics when they emerge from noise. This is illustrated on figure 25(*b*) ($U = 1.58U_L$): the two trajectories first diverge, then merge and lead to the fixed point. For higher upper plate velocity (figure 25*c*, $U = 2U_L$) the trajectories are completely different, but still lead to the same fixed point.

Far from the threshold ($U > 2.4U_L$), two different saturated waves were observed for the same flow conditions, corresponding to bistability. The first wave is dominated by the fundamental harmonic whereas the second wave is dominated by the second harmonic. The latter wave is reached after periodic energy exchange between A_2 and A_3 on the one hand, and between A_4 and A_5 on the other hand, while A_1 vanishes. Figure 25(*d*) shows, for $U = 2.43U_L$, two trajectories leading to each of the two fixed points. The observed saturated wave depends on random initial conditions which belong to the basin of attraction of one or other fixed point.

The experimental results can now be compared to numerical simulations of spatially periodic solutions of model equations describing long waves on sheared interfaces. The essential features of the observed waves are the following: asymmetry of the wave shape at the threshold of instability, linear dispersion, bistability and absence of chaotic behaviour under the explored flow conditions. The asymmetry of the wave shape can be related to the absence of reflectional invariance for the basic flow (the viscosity difference allows the right and left sides to be defined unambiguously). However, this asymmetry cannot be rendered by the KS equation, whose solutions resulting from the primary instability have reflectional invariance. The experimental observations can be better reproduced when a linear dispersive term $\eta_{,xxx}$ is taken into account (i.e. with the KdV–KS equation). Indeed, this term breaks the reflectional invariance and stabilizes the stationary solutions, as shown by Chang *et al.* (1993). Finally, the observed bistability can be related to numerical results obtained by Tilley, Davis & Bankoff (1994), for long waves in two-layer Poiseuille flow in an inclined channel. Their bistability, namely two travelling waves with different amplitudes, was exhibited from the '3KS equation', which includes the cubic nonlinearity $\eta^2\eta_{,x}$ to the KS equation (for horizontal channels, the 3KS equation is (16) with $T = M = 0$). This cubic nonlinearity breaks the same symmetry as the linear dispersive term, and corresponds in fact to nonlinear dispersion.

We thank J. Dusek and O. Thual for stimulating discussions, and D. Legendre for the direct numerical simulations of the basic flow. We are also grateful to J. J. Huc for his care in manufacturing the experimental device.

REFERENCES

CHANG, H. C., DEMEKHIN, E. A. & KOPELEVICH, D. I. 1993 Laminarizing effects of dispersion in an active-dissipative nonlinear medium. *Physica* D **63**, 299.

CHARLES, M. E. & LILLELEHT, L. U. 1965 An experimental investigation of stability and interfacial waves in a co-current flow of two liquids. *J. Fluid Mech.* **22**, 217.

CHARRU, F. 1991 Stabilité de l'interface entre deux fluides visqueux. Thèse de Doctorat, Institut National Polytechnique de Toulouse.

CHARRU, F. & FABRE, J. 1994 Long waves at the interface between two viscous fluids. *Phys. Fluids* **6**, 1223.

COHEN, B. I., KROMMES, J. A., TANG, W. M. & ROSENBLUTH, M. N. 1976 Non-linear saturation of the dissipative trapped-ion mode by mode coupling. *Nucl. Fusion* **16**, 971.

DEMEKHIN, E. A., TOKAREV, G. Y. & SHKADOV, V. YA. 1991 Hierarchy of bifurcations of space-periodic structures in a nonlinear model of active dissipative media. *Physica* D **52**, 338.

HINCH, E. J. 1984 A note on the mechanism of the instability at the interface between two shearing fluids. *J. Fluid Mech.* **144**, 463.

HOOPER, A. P. 1985 Long-wave instability at the interface between two viscous fluids: Thin layer effects. *Phys. Fluids* **28**, 1613.

HOOPER, A. P. & BOYD, W. G. C. 1983 Shear-flow instability at the interface between two viscous fluids. *J. Fluid Mech.* **128**, 507.

HOOPER, A. P. & BOYD, W. G. C. 1987 Shear flow instability due to a wall and a viscosity difference at the interface. *J. Fluid Mech.* **179**, 201.

HOOPER, A. P. & GRIMSHAW, R. 1985 Nonlinear instability at the interface between two viscous fluids. *Phys. Fluids* **28**, 37.

KAO, M. E. & PARK, C. 1972 Experimental investigation of the stability of channel flow. *J. Fluid Mech.* **52**, 401.

KELLY, R. E., GOUSSIS, D. A., LIN, S. P. & HSU, F. K. 1989 The mechanism for surface wave instability in film flow down an inclined plane. *Phys. Fluids* A **1**, 819.

KEVREKIDIS, I. G., NICOLAENKO, B. & SCOVEL, J. C. 1990 Back in the saddle again: a computer assisted study of the Kuramoto–Sivashinsky equation. *SIAM J. Appl. Maths* **50**, 760.

LIU, J., PAUL, J. D. & GOLLUB, J. P. 1993 Measurements of the primary instabilities of film flows. *J. Fluid Mech.* **250**, 69.

MAGNAUDET, J., RIVERO, M. & FABRE, J. 1995 Accelerated flows around a rigid sphere or a spherical bubble. Part 1. Steady straining flow. *J. Fluid Mech.* **284**, 97.

MANNEVILLE, P. 1990 *Dissipative Structures and Weak Turbulence.* Academic.

MELVILLE, W. K. 1983 Wave modulation and breakdown. *J. Fluid Mech.* **128**, 489.

NEWELL, A. C., PASSOT, T. & LEGA, J. 1993 Order parameter equations for patterns. *Ann. Rev. Fluid Mech.* **25**, 399.

RENARDY, Y. 1985 Instability at the interface between two shearing fluids in a channel. *Phys. Fluids* **28**, 3441.

RENARDY, Y. 1987 The thin layer effect and interfacial stability in a two-layer Couette flow with similar liquids. *Phys. Fluids* **30**, 1627.

RENARDY, Y. 1989 Weakly nonlinear behavior of periodic disturbances in two layer Couette–Poiseuille flow. *Phys. Fluids* A **1**, 1666.

SHLANG, T., SIVASHINSKI, G. I., BABCHIN, A. J. & FRENKEL, A. L. 1985 Irregular wavy flow due to viscous stratification. *J. Phys. Paris* **46**, 863.

SMITH, M. K. 1990 The mechanism for the long-wave instability in thin liquid films. *J. Fluid Mech.* **217**, 469.

TILLEY, B. S., DAVIS, S. H. & BANKOFF, S. G. 1994 Nonlinear long-wave stability of superposed fluids in an inclined channel. *J. Fluid Mech.* **277**, 55.

YIANTSIOS, S. G. & HIGGINS, B. G. 1988 Linear stability of plane Poiseuille flow of two superposed fluids. *Phys. Fluids* **31**, 3225.

YIH, C. S. 1967 Instability due to viscous stratification. *J. Fluid Mech.* **27**, 337.